Geochimica et Cosmochimica Acta xxx (xxxx) xxx

Contents lists available at ScienceDirect

Geochimica et Cosmochimica Acta

journal homepage: www.elsevier.com/locate/gca

Experimental investigation of the bonding of sulfur in highly reduced silicate glasses and melts

A. Pommier [a,*], M.J. Tauber [a,b], H. Pirotte [a,c], G.D. Cody [a], A. Steele [a], E.S. Bullock [a], B. Charlier [c], B.O. Mysen [a]

[a] Carnegie Institution for Science, Earth and Planets Laboratory, Washington, DC 20015, USA
[b] University of California San Diego, Department of Chemistry and Biochemistry, La Jolla, CA 92093, USA
[c] University of Liège, Department of Geology, Sart Tilman, Belgium

ARTICLE INFO

Associate editor: Sung Keun Lee

Keywords:
Mercury
Silicate glasses
Silicate melts
Sulfur
Impedance spectroscopy
NMR spectroscopy
Raman spectroscopy

ABSTRACT

Elucidating the role of sulfur on the structure of silicate glasses and melts at elevated pressures and temperatures is important for understanding transport properties, such as electrical conductivity and viscosity, of magma oceans and mantle-derived melts. These properties are fundamental for modeling the evolution of terrestrial planets and moons. Despite several investigations of sulfur speciation in glasses, questions remain regarding the effect of S on complex glasses at highly reducing conditions relevant to Mercury. Glasses were synthetized with compositions representative of the Northern Volcanic Plains of Mercury and containing quantities of S up to 5 wt %. Multiple spectroscopic methods and microprobe analyses were employed to probe the glasses, including *in situ* impedance spectroscopy at 2- and 4-GPa pressures and temperatures up to 1740 K using a multi-anvil press, ^{29}Si NMR spectroscopy, and Raman spectroscopy. Electrical activation energies (Ea) in the glassy state range from 0.56 to 1.10 eV, in agreement with sodium as the main charge carrier. The electrical measurements indicate that sulfide improves Na^+ transport and may overcome a known impeding effect of the divalent cation Ca^{2+}. The glass transition temperature lies between 700 and 750 K, and for temperatures up to 970 K Ea decreases (0.35–0.68 eV) and the conductivities of the samples converge (~5–8 × 10^{-3} S/m). At T_{quench}, the melt fraction is 50–70% and melt conductivity varies from 0.7 to 2.2 S/m, with the sample containing 5 wt% S the most conductive among the set. ^{29}Si NMR spectra reveal that a high fraction of S bonds with Si in these complex glasses, a characteristic that has not been recognized previously. Raman spectra and maps reveal regions rich in Ca–S or Mg–S bonds. The evidence of sulfide interactions with both Si and Ca/Mg suggest that alkaline earth sulfides can be considered weak network modifiers in these glasses, under highly reduced conditions.

1. Introduction

Sulfur is a major volatile component in terrestrial magmas. The presence of sulfur can influence the structure of silicate melts and glasses (e.g., O'Neill and Mavrogenes, 2002; Fleet et al., 2005; Tsujimura et al., 2004; Klimm and Botcharnikov, 2010) affecting transport properties such as diffusivity (Lierenfeld et al., 2018), thermal conductivity (Lonergan et al., 2020), and viscosity (Mouser et al., 2021). Understanding the effect of sulfur on these properties at the temperatures, pressures, and redox conditions relevant to planetary interiors is an important part of modeling the composition and dynamics of terrestrial planets and moons. High S concentrations (up to 4 wt%), together with low FeO content (≤2–3 wt%) were measured at the surface of Mercury during the MESSENGER mission by using gamma-ray, X-ray, and ultraviolet – near-infrared reflection spectroscopy (Nittler et al., 2011, 2018; Zolotov et al., 2013; Evans et al., 2012; Izenberg et al., 2014; Weider et al., 2015; Peplowski et al., 2015; McCoy et al., 2018). These data are consistent with a highly reducing environment (<IW-3, with IW the iron-wüstite oxygen fugacity buffer; McCubbin et al., 2012; Zolotov et al., 2013; Namur et al., 2016a). These conditions are thought to have affected planetary differentiation and magmatic processes (e.g., Malavergne et al., 2010; Charlier and Namur, 2019; Renggli et al., 2022). However, the effect of highly reduced S-rich magmas on the dynamics that shaped the planet remains largely unknown.

In natural silicate glasses and melts, sulfur can exist in a wide range of oxidation states, from S^{2-} to S^{6+} (e.g., Carroll and Rutherford, 1988;

* Corresponding author.
E-mail address: apommier@carnegiescience.edu (A. Pommier).

https://doi.org/10.1016/j.gca.2023.10.027
Received 5 July 2023; Accepted 24 October 2023
Available online 4 November 2023

Wilke et al., 2011; O'Neill and Mavrogenes, 2002). At an oxygen fugacity (fO_2) above that of the nickel-nickel oxide oxygen buffer, S^{6+} in the form of sulfate (SO_4^{2-}) is dominant, whereas at very low fO_2 values relevant to Mercury magmas, sulfide (S^{2-}) is the predominant sulfur species (e.g., Jugo et al., 2010). The following equilibrium characterizes the displacement of oxide for sulfide in a melt (Fincham and Richardson, 1954; Baker and Moretti, 2011):

$$\frac{1}{2}S_2^{gas} + O^{2-,melt} = \frac{1}{2}O_2^{gas} + S^{2-,melt} \quad (1)$$

For fO_2 values significantly below the IW buffer, the maximum concentration of S^{2-} in a silicate melt (sulfide saturation) increases as oxygen fugacity decreases (e.g., O'Neill and Mavrogenes, 2002; Namur et al., 2016a). Therefore, the remarkably low fO_2 conditions in Mercury have been invoked to explain the substantial solubility of sulfide in its lavas (Nittler et al., 2011; Namur et al., 2016a). Sulfide has an affinity for divalent cations (Ca^{2+}, Mg^{2+}, Fe^{2+}), forming complexes in various glasses (O'Neill and Mavrogenes, 2002; Fleet et al., 2005; Namur et al., 2016a; Anzures et al., 2020). Additional processes which may induce the formation of Ca or Mg sulfides at the surface of Mercury have been suggested, such as gas–solid interactions during volcanic and impact processes (Renggli et al., 2022). SiS_2 is another compound that can form during volcanic degassing at the surface of this planet (Iacovino et al., 2023).

Our current understanding of the effect of S on the structure of silicate glasses and melts has benefitted significantly from industry-related research on simple binary or ternary systems. As reviewed elsewhere (Wilke et al., 2011), various spectroscopic techniques have been used to investigate the speciation and bonding of sulfur in alkali silicate glasses, including Raman scattering (Asahi et al., 1999; Tsujimura et al., 2004; Klimm and Botcharnikov, 2010; Klimm et al., 2012; Namur et al., 2016a; Watson and Martin, 2017; Lonergan et al., 2020), nuclear magnetic resonance (NMR) (Tsujimura et al., 2004; Watson and Martin, 2017), X-ray photoelectron spectroscopy (Asahi et al., 1999), and X-ray absorption near-edge structure (XANES) spectroscopy (Fleet et al., 2005; Klimm et al., 2012; Anzures et al., 2020). Generally, simple glass compositions were targeted in these studies, and further investigations are needed to elucidate the role of S in complex (natural) glasses and under highly reducing conditions relevant to Mercury.

Among the spectroscopic techniques commonly used to study complex S-bearing glasses and melts, ^{29}Si NMR spectroscopy is outstanding for identifying the various nearest neighbors of Si and for providing essential information about glass polymerization. The speciation of silicon is of particular interest, with the extent of polymerization commonly denoted by the parameter Q^n, where Q refers to a tetrahedrally-bonded Si species and an integer n (1–4) quantifies the number of bridging oxygen atoms (e.g., Stebbins, 1987; Engelhardt and Michel, 1987; Maekawa et al., 1991). Raman spectroscopy is another powerful probe of silicate glasses, including those bearing S (Wilke et al., 2011). This technique has been used to probe sulfide compositions in natural samples (Avril et al., 2013), and identify S complexes with Mg^{2+} and Ca^{2+} in the structure of highly reduced silicate melts (Namur et al., 2016a).

Knowledge of the transport properties (such as viscosity and electrical conductivity) of such glasses and melts at conditions relevant to Mercury is limited. Results from viscosity experiments on highly reduced S-bearing andesitic glasses up to 6.2 GPa and 2000° C revealed a decrease in viscosity with the addition of S (Mouser et al., 2021). The mechanism for the decrease is uncertain, however, the generally weaker interaction of S^{2-} relative to O^{2-} with cations such as $Si^{2+,4+}$ and Ca^{2+} could influence viscosity. Additionally, low viscosity values at low fO_2 can perhaps be explained by the decreased valence of Si and Ti, thereby decreasing polymerization (Mouser et al., 2021). Impedance spectroscopy is sensitive to the short- and long-range motion of charged species and yields insights that are complementary to those from other spectroscopic techniques and viscosity experiments. For example, a study of S-bearing Li silicate glasses (Tatsumisago et al., 2000) benefitted from electrical measurements, combined with ^{29}Si NMR spectroscopy and XPS. However, the previous electrical studies of S-bearing, alkali silicate glasses (e.g., Ravaine, 1980 and references therein; Hayashi et al., 1998; Tatsumisago et al., 2000; Minami et al., 2000) were restricted to simple systems and oxysulfides at 1 atm. To elucidate planetary interiors, measurements of electrical and other transport properties of complex, sulfide-bearing silicate glasses are needed at high pressures and temperatures.

In this study, we investigate the role of sulfur in highly reduced complex silicate glasses and melts. Several spectroscopic techniques are applied to probe the electrical properties (impedance spectroscopy) and molecular structure (^{29}Si NMR spectroscopy and Raman spectroscopy) of these glasses. Electron microprobe analyses complement the characterization of the samples. The different insights gained from each technique combine to elucidate the bonding of sulfur in highly reduced silicate glasses.

2. Experimental and analytical techniques

2.1. Sample preparation

The starting glasses were synthesized from powders representative of the compositions from the low-Mg Northern Volcanic Plains (termed NVP) in the Borealis Planitia region on Mercury (Weider et al., 2015; Namur and Charlier, 2017; Vander Kaaden et al., 2017). Magmas from this location are rich in Mg, alkali metals, and S, but are depleted in Al, Ca and Fe compared with Earth basalts (e.g., Peplowski et al., 2014, 2015). High-purity oxides (TiO_2, Al_2O_3, Cr_2O_3, MnO, MgO, $CaSiO_3$, Na_2SiO_3, $K_2Si_4O_9$, $AlPO_4$) were mixed with ethanol in an agate mortar. Different amounts of S, in the form of CaS, were added to the powders (Table 1). Iron was added as Fe to two batches. The powders were dried in an oven at 393 K and stored in a desiccator until use.

Starting glasses were obtained by loading the powders into graphite capsules and melting with a multi-step process. The capsule was first placed in a silica tube under vacuum and heated at 393 K for about 15 h. The tube containing the sample was then sealed while still under vacuum using an oxy-acetylene torch, and placed in a box oven at 1573 to 1673 K for 0.75–1.5 h (Table 1). The pressure is estimated to be slightly above 1 bar based on slight inflation of some silica tubes. The redox conditions of the sample are expected to be close to the C-CO redox buffer at the oven temperature. Therefore, at the 1573–1673 K temperatures and ~1 bar pressure of the syntheses, the fO_2 values were approximately six log units lower than those of the iron-wüstite buffer ($\Delta IW \approx -6$) (Herd, 2008 using Eugster and Wones, 1962 and Darken and Gurry, 1945). Samples were quenched by dropping the silica tubes inside a water-filled beaker. The quenching rate is estimated to be >200–300 K/s. Upon opening the silica tubes, representative samples showed evidence of CO and H_2S gases. Glass cylinders were retrieved by removing the graphite capsule, and have a diameter of 1.5 mm and length of ~1–2 cm.

Table 1
Starting materials and conditions of glass synthesis experiments (P = 1 atm).

Glass sample	Added materials (wt.%)		Experimental conditions[a]	
	CaS	Fe	Temperature (K)	Duration (hr)
VT42	0	10	1623	1.0
VT53	0	0	1573	1.5
VT56	0	0	1623	1.0
VT46	7	10	1623	1.0
VT47	7	0	1623	1.0
VT48	7	0	1573	1.0
VT54	12	0	1573	1.5
VT55	15	0	1673	0.75
VT52	30	0	1623	1.0

[a] Graphite capsules for all annealing.

The synthesized S-bearing glasses were reddish brown in color. Optical microscopic examinations do not reveal the presence of crystals. Scarce metal-rich micro-droplets are observed in a few samples. Bubbles are present in some glasses; in this case, the glass cylinder was pulverized for electrical experiments to avoid artifacts in the measurement of bulk electrical properties. Nine starting compositions were synthesized, with S content varying from 0 to 4.8 wt%. Because the starting glasses were synthesized in graphite capsules, fine graphite particles are observed on the surface of most glass cylinders.

Starting glasses and samples retrieved after electrical experiments under pressure and temperature were analyzed using the electron microprobe to characterize the phases, composition, and texture. Analyses were performed with a JEOL 8530F field-emission electron microprobe, with an acceleration voltage of 15 kV and a sample current of 20 nA. Integration times were 20 s on peak and 10 s on background, except for Na and P, that were analyzed with 50% shorter times. The beam was slightly defocused (~5 μm). The following standards were used: basaltic glass (for measuring Na, Mg, Ti, Ca, Al, Si, Fe), ilmenite (Mn), orthoclase (K), pyrite (S), and apatite (P). In addition to spot analyses on the silicate and sulfide phases, energy dispersive spectroscopy (EDS) and wavelength dispersive spectroscopy (WDS) were used to obtain chemical maps of selected samples. High-resolution WDS maps used a 1-μm diameter beam and a 20-ms dwell time. Each spectroscopic technique used to study the glasses (Table 2) is described in the following subsections.

2.2. Impedance spectroscopy measurements under pressure and temperature

Electrical experiments were carried out at 2 GPa (except for one experiment performed at 4 GPa) under quasi-hydrostatic conditions in a 1,100-ton Walker-type Rockland multi-anvil press. Experimental conditions are listed in Table 2. Pressure was applied using eight tungsten carbide cubes with corner-truncated edge length of 8 mm and MgO octahedral pressure media with an edge length of 14 mm. All MgO parts were fired at ≥1273 K and stored in a desiccator until use. Two types of electrical cell assembly were used, depending on the temperature range of the electrical measurements (Appendix B, Fig. S1). For experiments quenched at a temperature slightly above the glass transition of the sample (low-T experiments), the cell assembly was composed of three MgO sleeves, with the middle one containing the sample, and of two high-purity Fe disks (Pommier and Leinenweber, 2018). The sample used for these low-T experiments was a glass cylinder with the same diameter as the synthesized glasses (1.5 mm). For experiments quenched at a temperature for which the sample was partially molten (high-T experiments), the electrical cell assembly consisted of three MgO sleeves, with the middle one comprised of three alumina rings separated from each other by two high-purity Fe disks (Saxena et al., 2021). The starting material used for these high-T experiments was glass powder. The middle alumina ring contained the sample, and the design prevented molten material from escaping the cell. With either assembly, the sample was heated by applying a current to the surrounding Re foil, and temperature was monitored using one of two Type-C thermocouples ($W_{95}Re_5$-$W_{74}Re_{26}$). Each thermocouple contacted one of two Fe-metal disks that were electrodes for impedance measurements.

The cell assembly was initially compressed to the target pressure at room temperature, and the temperature was then increased in 25 K increments. Impedance data were collected during heating. Fig. S2 (Appendix B) shows the temperature–time and the temperature-power paths for all experiments. The pressure remained within (±) 2% of the target value throughout the heating cycle. All experiments were quenched by turning off the power to the heater at a temperature below the melting point of the Fe electrodes (~1850 K; e.g., Buono and Walker, 2011). After decompression, the electrical cell was mounted in an epoxy resin, sliced longitudinally, and polished to expose the surface of the sample for chemical and textural microprobe analyses.

Electrical measurements consisted of 4-electrode impedance spectroscopy (Ametek 1260 Solartron Impedance/Gain-Phase Analyzer). To measure the complex impedance, a potential with DC component 1 V and AC amplitude ≤ 1 V was applied from 1 MHz to ~1 Hz. The sample response was not sensitive to variation in AC amplitude between 200 mV and 1 V. The complex impedance Z is composed of a real part Z' and an imaginary part Z″. The Z' value determined at relatively low frequency, either as a local minimum in the complex impedance plane, otherwise as an intersection or extrapolated intersection with the real axis, is considered the bulk electrical resistance (R). The sample resistance R_{sample} is obtained from R after removing very minor contributions from the alumina ring (electrically in parallel with the sample in the high-T assembly; Fig. S1) and the two electrode disks (electrically in series with the sample). Reproducibility was checked by (1) making multiple measurements during an experiment at defined temperature, and (2) duplicating electrical experiments for glass VT55 at overlapping temperature ranges using a different electrical cell (BBC12 and BBC18 experiments, Table 2).

The electrical conductivity σ of the sample at each temperature is calculated from R_{sample}:

$$\sigma = \frac{1}{R_{sample} \times G} \quad (2)$$

In Eq. (2), the geometric factor G is the ratio (electrode disk area, πr^2) / (sample thickness, l). The error in each conductivity value is typically a few percent (Appendix B, Supplementary material).

2.3. ^{29}Si NMR spectroscopy

^{29}Si NMR spectra were acquired on starting glasses VT53, VT48, VT52, and VT54 using a solid-state NMR spectrometer (Chemagnetics Infinity). The resonant frequency of ^{29}Si is 59 MHz in the 7-tesla static field. The synthesized glasses were crushed into a powder and loaded into a 5-mm diameter rotor. Spectra were acquired with a 1.3-μs pulse width, corresponding to a 30° nutation angle. The iron content in those samples analyzed by NMR spectroscopy (≤0.02 wt% Fe_2O_3) is below the

Table 2
Summary of the different measurements performed on starting glasses.

Glass	Impedance spectroscopy				EMPA	NMR spectroscopy	Raman spectroscopy
	Experiment	Starting material	Pressure (GPa)	T range (K)			
VT42 (S free)	BBC21	Powder	2	1473–1673	SG and QM*	–	SG
VT46	BBC22	Powder	2	1578–1738	SG and QM	–	QM
VT47	BBC15	Powder	2	1388–1619	SG and QM	–	–
VT48	BBC16	Cylinder	2	573–874	SG and QM	SG	QM
VT52	BBC17	Powder	2	623–1657	SG and QM	SG	SG and QM
VT53 (S free)	BBC13	Cylinder	2	598–1031	SG and QM	SG	–
VT54	BBC14	Cylinder	2	523–973	SG and QM	SG	–
VT55	BBC12, BBC18	Cylinder, powder	2, 2	475–944, 673–1593	SG and QM	–	SG and QM
VT56 (S free)	BBC10, BBC19	Powder, powder	2, 4	593–1669, 625–1585	SG and QM	–	SG

* SG: analyses on starting glass; QM: analyses on quenched material from electrical experiment.

levels previously reported to cause significant shortening of T1 relaxation times (Maekawa et al., 1991; Ackerson et al., 2020). However, the presence of paramagnetic Mn^{2+} (0.04–0.32 wt% MnO) is comparable to quantities known to decrease T1 significantly (Scholz and Thomas, 1995) thereby allowing a short (2-s) recycle delay without saturation. The magic-angle spinning (MAS) frequency ($\omega_r/2\pi$) was 8 kHz. The number of acquisitions was 40,000 × 4. The chemical shifts were referenced to the ^{29}Si frequency of tetramethylsilane (TMS) defined as 0 ppm. NMR spectra were not acquired for the quenched samples from electrical experiments, because the amount of material in the multi-anvil cell assembly was insufficient.

2.4. Raman spectroscopy

Raman spectra were collected on selected starting glasses and quenched samples from electrical experiments (Table 2). Methods used in this study are similar to those outlined in Steele et al. (2007, 2012). Two scanning near-field optical microscope systems (WITec Alpha) were

Table 3
Summary of electron microprobe analyses (in wt.%) of starting glasses and quenched samples after electrical experiments.

Silicate analyses		Na_2O	MgO	TiO_2	CaO	Al_2O_3	SiO_2	FeO	MnO	K_2O	S	P_2O_5	Total
VT42	*Starting glass*												
	average (9)*	5.09	10.7	0.39	5.59	14.3	64.2	0.62	0.32	0.18	0.00	0.01	101.4
	std dev.	*0.08*	*0.3*	*0.06*	*0.13*	*0.3*	*0.7*	*0.23*	*0.04*	*0.01*	*0.00*	*0.01*	
	BBC21, 2 GPa, 1673 K												
	average (58)	5.05	10.3	0.38	5.40	14.2	65.1	1.23	0.29	0.19	0.00	–	102.2
	std dev.	*0.30*	*0.5*	*0.02*	*0.20*	*0.5*	*1.0*	*0.21*	*0.03*	*0.03*	*0.00*	–	
VT46	*Starting glass*												
	average (6)	5.22	10.6	0.35	5.76	14.7	62.4	1.29	0.20	0.36	0.12	0.04	101.0
	std dev.	*0.29*	*0.3*	*0.03*	*0.28*	*0.3*	*0.9*	*0.47*	*0.04*	*0.02*	*0.02*	*0.05*	
	BBC22, 2 GPa, 1738 K												
	average (68)	4.99	9.16	0.36	5.40	15.0	64.1	1.27	0.19	0.40	0.15	–	101.1
	std dev.	*0.47*	*1.64*	*0.02*	*0.18*	*0.6*	*0.9*	*0.34*	*0.02*	*0.05*	*0.05*	–	
VT47	*Starting glass*												
	average (9)	4.27	11.4	0.41	5.92	14.8	62.4	0.02	0.27	0.32	1.19	0.17	101.1
	std dev.	*0.33*	*0.9*	*0.08*	*0.29*	*0.6*	*0.6*	*0.02*	*0.13*	*0.04*	*0.74*	*0.10*	
	BBC15, 2 GPa, 1619 K												
	average (30)	5.00	9.40	0.32	5.30	14.1	63.8	0.07	0.21	0.41	2.11	0.19	101.0
	std dev.	*0.52*	*1.83*	*0.07*	*0.47*	*1.2*	*1.0*	*0.04*	*0.06*	*0.08*	*0.40*	*0.06*	
VT48	*Starting glass*												
	average (6)	5.05	10.2	0.32	5.45	14.4	63.6	0.01	0.13	0.37	1.71	0.21	101.5
	std dev.	*0.16*	*0.3*	*0.06*	*0.31*	*0.6*	*1.0*	*0.02*	*0.02*	*0.01*	*0.07*	*0.04*	
	BBC16, 2 GPa, 874 K												
	average (29)	4.99	10.4	0.36	5.39	14.3	64.3	0.01	0.16	0.37	1.77	0.22	102.2
	std dev.	*0.16*	*0.8*	*0.04*	*0.40*	*0.6*	*1.5*	*0.01*	*0.04*	*0.03*	*0.10*	*0.04*	
VT52	*Starting glass*												
	average (6)	4.57	8.61	0.28	13.1	12.8	59.2	0.02	0.04	0.33	3.82	0.07	102.9
	std dev.	*0.27*	*0.36*	*0.04*	*0.9*	*0.2*	*0.7*	*0.01*	*0.02*	*0.04*	*0.72*	*0.06*	
	BBC17, 2 GPa, 1657 K												
	average (25)	4.45	8.41	0.22	15.1	12.2	57.0	0.05	0.04	0.35	5.62	0.07	103.6
	std dev.	*0.15*	*0.82*	*0.03*	*0.3*	*0.2*	*0.4*	*0.05*	*0.02*	*0.06*	*0.93*	*0.05*	
VT53	*Starting glass*												
	average (15)	6.30	10.1	0.38	6.30	15.5	61.8	0.01	0.32	0.16	0.00	0.15	101.1
	std dev.	*0.08*	*0.1*	*0.02*	*0.09*	*0.1*	*0.4*	*0.01*	*0.03*	*0.01*	*0.00*	*0.02*	
	BBC13, 2 GPa, 1031 K												
	average (6)	5.84	9.48	0.41	5.62	14.8	64.6	0.14	0.33	0.18	0.01	–	101.4
	std dev.	*0.09*	*0.49*	*0.04*	*0.38*	*0.6*	*1.5*	*0.16*	*0.02*	*0.01*	*0.00*	–	
VT54	*Starting glass*												
	average (7)	4.46	9.59	0.34	8.49	13.6	61.7	0.02	0.08	0.34	4.20	0.19	103.0
	std dev.	*0.22*	*0.35*	*0.07*	*0.31*	*0.4*	*0.8*	*0.02*	*0.01*	*0.02*	*0.28*	*0.05*	
	BBC14, 2 GPa, 973 K												
	average (7)	4.95	8.79	0.33	7.35	11.0	62.4	0.01	0.06	0.36	4.11	–	99.3
	std dev.	*0.10*	*0.48*	*0.02*	*0.49*	*0.3*	*1.9*	*0.02*	*0.02*	*0.03*	*0.18*	–	
VT55	*Starting glass*												
	average (8)	5.31	10.1	0.31	10.4	14.7	55.9	0.00	0.18	0.37	4.79	0.11	102.2
	std dev.	*0.13*	*0.1*	*0.02*	*0.3*	*0.3*	*0.2*	*0.00*	*0.04*	*0.01*	*0.33*	*0.05*	
	BBC12, 2 GPa, 944 K												
	average (50)	5.14	10.2	0.34	9.93	14.6	57.9	0.02	0.21	0.37	4.54	0.14	103.4
	std dev.	*0.10*	*0.2*	*0.02*	*0.15*	*0.2*	*0.4*	*0.02*	*0.03*	*0.02*	*0.23*	*0.13*	
	BBC18, 2 GPa, 1593 K												
	average (29)	5.05	10.3	0.29	10.5	14.7	57.4	0.04	0.17	0.42	4.61	0.12	103.5
	std dev.	*0.34*	*0.7*	*0.05*	*0.3*	*0.2*	*0.5*	*0.02*	*0.10*	*0.08*	*0.73*	*0.07*	
VT56	*Starting glass*												
	average (17)	6.00	11.7	0.38	6.28	15.2	61.4	0.02	0.32	0.17	0.00	0.12	101.6
	std dev.	*0.06*	*0.1*	*0.02*	*0.08*	*0.4*	*0.5*	*0.02*	*0.03*	*0.01*	*0.00*	*0.02*	
	BBC19, 4 GPa, 1585 K												
	average (25)	5.51	9.86	0.41	5.37	14.0	64.8	0.04	0.31	0.17	0.00	–	100.5
	std dev.	*0.31*	*0.60*	*0.04*	*0.32*	*0.8*	*1.7*	*0.02*	*0.03*	*0.05*	*0.00*	–	

Sulfide analyses		Fe	S	Si	Mg	Ca	Mn	Total
VT46	*BBC22, 2 GPa, 1738 K*							
	average (5)*	68.7	27.9	0.08	0.01	0.03	0.08	96.8
	std dev.	*2.71*	*2.14*	*0.03*	*0.01*	*0.04*	*0.05*	

* Number of analyses. Each analysis was performed using a 5-μm defocused beam.

employed, both with confocal Raman spectroscopic imaging capability. The excitation wavelength was 532 nm. The power at the sample was 0.3 to 1 mW. Spectra were collected without analysis of polarization. The excitation laser was focused either at the surface of the sample, or several μm below it. The entrance to a 50-μm optical fiber served as the confocal aperture. The scattered light was dispersed with a 600-groove/mm grating, and Raman spectra in the 200–3600 cm^{-1} range were acquired with an integration time of 1 to 6 s per pixel. Imaged areas were typically (20–50 μm) × (20–50 μm), and the spatial resolution was 1 μm. Raw spectra were first processed using WITec software (Project Plus version 5.2) to remove any signals from cosmic rays, or to subtract a broad emission background (when present) using the shape function (curve diameter 50 cm^{-1}). Principal component analysis (PCA) was also performed on the full set of Raman spectra within selected imaged areas, using the WITec software.

3. Results and discussion

3.1. Chemical composition

The chemical composition of the synthesized glasses is summarized in Table 3. The S concentration can be categorized in three groups: samples with 0.0–0.1 wt% S (VT42, VT53, VT56, VT46); those with 1–2 wt% S (VT47, VT48) and those with 3.8–4.8 wt% S (VT52, VT54, VT55). The fact that ~5 wt% S was the maximum amount, even upon addition of 12–30 wt% CaS, is consistent with sulfur solubility at an fO_2 of −6 relative to IW and the temperatures of the syntheses (see Fig. 3 of Namur et al., 2016a and Fig. 2 of Anzures et al., 2020). Samples with added iron (VT42, VT46) were analyzed to have 0.6 or 1.3 wt% FeO. The amounts of Ti and K are small (<0.5 wt% TiO_2 or K_2O) for all samples. Likewise, the concentrations of Mn are small (0.04–0.32 wt% MnO) but even these quantities likely affect the NMR spectroscopy, as mentioned above.

Relative molar quantities of the constituents are fundamentally important and can be summarized as follows. The sulfide-free (VT42, 53, 56) and low-S (VT46, 47, 48) glasses have a combined average mol.% composition of 5 Na_2O, 16 MgO, 6 CaO, and 9 Al_2O_3, 63 SiO_2. The average mol.% composition of S-rich (VT54, 55, 52) glasses, assuming all cations as oxides and excluding S from the analysis, is 5 Na_2O, 14 MgO, 12 CaO, 8 Al_2O_3, and 61 SiO_2. These glasses contain 12 to 16 mol.% S relative to Si, which replaces O. Alkaline earth metals Mg^{2+} and Ca^{2+} are the dominant cations (other than Si^{4+}) in the glasses; combined, they are on average 35 mol.% of Si for the samples with low or no S, and 43 mol.% of Si for the S-rich samples. Na^+ is the only alkali cation with significant quantity (16 mol.% relative to Si). Network former Al_2O_3 is ~14 mol.% of SiO_2.

Back-scattered electron (BSE) images of selected samples from electrical experiments are shown in Fig. 1. The sample diameter remained identical during the experiment, but because Fe disks deformed slightly during compression (Fig. 1**A**), the sample thickness considered in Eq. (2) is an average value. Crystals are visible in the samples quenched at high temperature (high-T cell assembly) (Fig. 1**B**) and indicate a partially molten state at the quenching temperature. The olivine crystals observed in the retrieved samples are small and characterized by euhedral shapes with well-developed faces, and are thought to have formed prior to quenching (crystals grown during the quench would have skeletal shapes). A partially crystallized state after quenching also agrees with previous phase-equilibria experiments that indicate a liquidus temperature of ~1673 K for the S-bearing NVP composition at 1 GPa (Namur et al., 2016b). From analysis of the BSE images (ImageJ software; see Fig. S3 (Appendix B) for example), the melt fraction in samples for the high-T experiments is estimated to be ~0.5–0.7, with the lowest values for the S-free glasses. In contrast, samples quenched at low temperature (cells with an MgO sample sleeve) preserved a clean glass texture (Fig. 1**C**). Only two samples have iron sulfides (BBC21 and BBC22), as illustrated in Fig. 1**D** for BBC22. These samples contain the highest Fe content (reported as 1.2 and 1.3 wt% FeO in Table 3). In addition to Fe and S, these sulfides also contain some silicon and trace amounts of phosphorus. WDS maps for this sample (Fig. S4**A**, Appendix B) show that Fe is not in the silicate phase, or it is below the detection limit of the electron microprobe analyses.

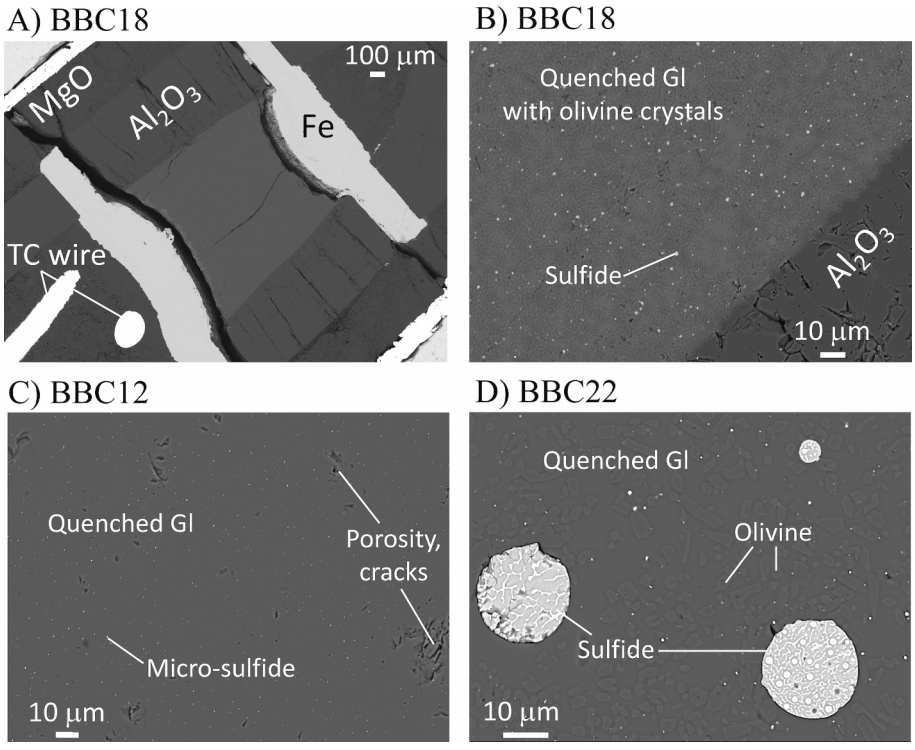

Fig. 1. Back-scattered electron (BSE) images of selected quenched samples from electrical experiments: A) and B) BBC18 (glass VT55 quenched at 1593 K showing the presence of olivine crystals), C) BBC12 (glass VT55 quenched at 944 K), and D) BBC22 (glass VT46 quenched at 1738 K).

The bulk composition of quenched samples after electrical experiments is in good agreement with that of the starting glasses (Table 3). Most importantly, sulfur was maintained in the samples even at high temperature. The contamination of the samples by the middle sleeve (MgO ring for the low-T experiments, alumina ring for the high-T experiments) is insignificant, with an Mg-rich or Al-rich thin spinel layer limited to a few μm in thickness located at the MgO-sample or alumina-sample interface, respectively (Fig. 2). This layer is formed by the diffusion of Mg or Al into the sample at elevated temperature. One exception is sample BBC22 (using Fe-bearing glass VT46), where a few distinct crystals are observed at the alumina-sample interface (Fig. S4**b**, Appendix B). Chemical analyses suggest that this S-free silicate phase is rich in Al, Mg, Ca, Na and Fe (Table 3), consistent with an augite (porricin, or grünblende). Iron from the electrodes incorporates in the sample, but only over a restricted range (up to ~50 μm from the interfaces) (Fig. 2). The chemical interactions between the electrode disks or the sample sleeve and the sample have a negligible effect on the bulk electrical measurements because of the limited thickness of the contaminated regions.

Significant compositional variation is observed in the starting glasses and remains in the quenched samples. The example of BBC16, quenched at 874 K, is shown in Fig. 3. For traverses across the sample diameter, the variation in content (wt.%) is: S, from 1.2 to 2.7; Na_2O, from 4 to 5.4; MgO, from 7.5 to 12; CaO, from 3.2 to 6.4; and SiO_2, from 58 to 68. WDS maps of samples also reveal some spatial variation in chemical content (Fig. 3). For samples quenched at high temperatures such as BBC18 (Fig. 2) there is similarly significant variation in chemical content across the sample, e.g., S, 2 to 6 wt%; MgO, 8 to 13 wt%. Spatial heterogeneity is common in alkaline silicate glasses but is typically minimized if alumina is present, as in our glasses. The specific causes for the heterogeneity within the glasses of the present study are not yet known. We note that the impedance and NMR measurements probe the samples as a whole, and the impact of spatial heterogeneity was not analyzed.

3.2. Impedance spectroscopy

Examples of impedance spectra for different samples at selected temperatures are presented in Fig. 4. The electrical resistance is determined from the low frequency portion (right side) of a relevant arc in the complex impedance plane, as described above. At low temperature, one impedance arc is observed for all samples as is typical of semiconductors (Fig. 4**a** and 4**b**). At high temperature (>1373 K), the sample resistance is derived from the second impedance arc at lower frequency (e.g., see arrows marking Z' positions in Fig. 4**c**). For all samples, resistance decreases with increasing temperature.

The electrical conductivity during heating of all glass samples is presented in Fig. 5. For each composition, conductivity increases non-linearly by more than four log units over the T range under consideration. In both the glassy and partially molten states, the S-rich samples are generally most conductive though there are exceptions. Given the addition of sulfide as CaS, S-rich samples also have relatively high Ca content. Some divalent cations, including Ca^{2+}, are known to impede alkali transport in silicate glasses and melts (e.g., Doremus, 1994; Shelby, 2020). It is likely that the S-rich samples would have greater conductivity if the Ca^{2+} content were the same as in the samples without S.

At temperatures below 700–750 K, the conductivity of most samples tracks reasonably well with the Arrhenius equation,

$$\sigma = \sigma_0 \times exp\left(\frac{-\Delta H}{RT}\right) \quad (3)$$

with σ_0 the pre-exponential term and ΔH the activation energy. Previous studies of alkali silicate glasses showed that the approach developed for ionic crystals can be applied to explain the physical significance of σ_0 and ΔH (Souquet and Perera, 1990; Caillot et al., 1994; Souquet et al., 1998). The formation of charge carriers in silicate glasses is similar to the formation of a Frenkel defect, and the thermally activated diffusion of charge carriers involves interstitial jumps (e.g., Souquet and Perera, 1990). In our glasses, ΔH ranges from 0.56 to 1.10 eV. The highest ΔH values are observed for S-free samples (VT42, VT56; Table 4), except for VT53 (0.63 eV). The lowest values of ΔH (0.54, 0.55 eV for samples VT54, VT55 respectively) are found with samples containing 4–5 wt% S. Although the results show a tendency for sulfide to decrease ΔH, several factors prevent us from claiming a systematic correlation for these glasses: (1) sulfide content is limited to <5%, an amount that constrains the extent of change in conductivity, (2) variation of other elements (particularly Ca^{2+}) can influence conductivity, and (3) there is a possible interference from carbon (see below). Despite these complications, a variety of synthetic systems have demonstrated that glasses with sulfide can greatly improve transport of alkali cations relative to those with oxide, for example a 10× greater conductivity at 100 °C, and significantly lower activation energy, for Na_2S-SiS_2 versus Na_2O-SiO_2 (Ribes et al., 1979); 100× greater conductivity and much lower activation energy for $0.6Li_2S{\cdot}0.4\ SiS_2$ versus $60\%(0.6Li_2S{\cdot}0.4\ SiS_2) + 40\%(Li_4SiO_4)$

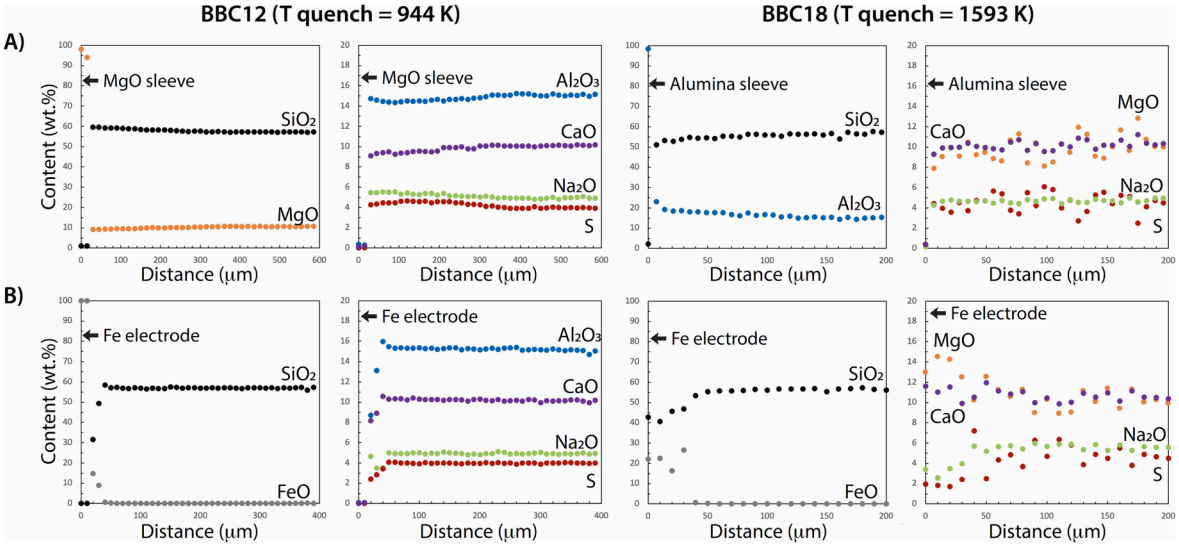

Fig. 2. Electron microprobe traverses for samples BBC12 and BBC18 (VT55 glass). A) Sample sleeve-sample traverses, with the sample sleeve being either MgO (BBC12) or Al_2O_3 (BBC18). B) Fe electrode-sample traverses.

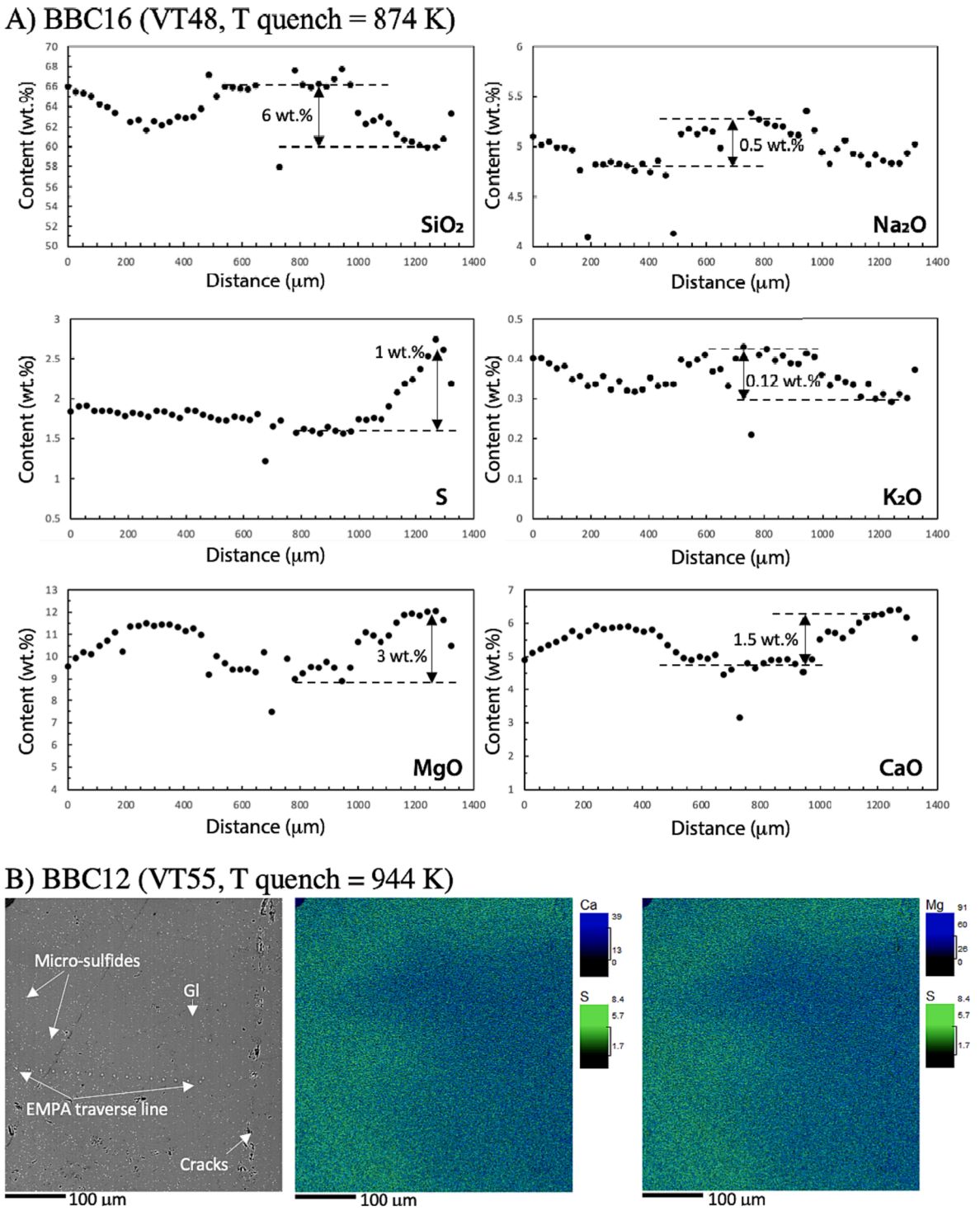

Fig. 3. Chemical variations across selected quenched samples. A) EMPA traverses across sample BBC16 (glass VT48) quenched at 874 K. B) Back-scattered electron (BSE) image and wavelength dispersive X-ray spectroscopy (WDS) maps of S, Ca, and Mg across sample BBC12 (glass VT55). The color scale bars reflect the number of counts for each element considered.

(Hirai et al., 1995; Minami et al, 2000); 100× greater conductivity of lithium sulfide + SiS_2 versus the oxide counterparts (Pradel and Ribes, 2014); and similar comparisons (Martin, 2016). The glasses in the present work generally contain much less sulfide and are prepared in a more reducing environment than these examples, nevertheless the tendency for sulfide to enhance conductivity and lower activation energy appears to be consistent with prior studies. The trend can be readily explained in terms of weaker coulombic interactions between sulfide and alkali ions relative to oxide and alkali ions, because sulfide has a larger ionic radius. Coulombic interactions are weakened further in sulfide-bearing samples because the larger relative dielectric permittivity, a consequence of the greater polarizability of S^{2-} versus O^{2-} (Martin, 2016).

Comparisons with previous electrical studies of natural silicate glasses below the glass transition temperature are limited because the effect of sulfide has not been explored, and the conditions of prior studies involving sulfur tend to be significantly less reducing than in the present study. Dry and hydrous complex silicate glasses in oxidizing environments show slightly lower conductivities than our samples

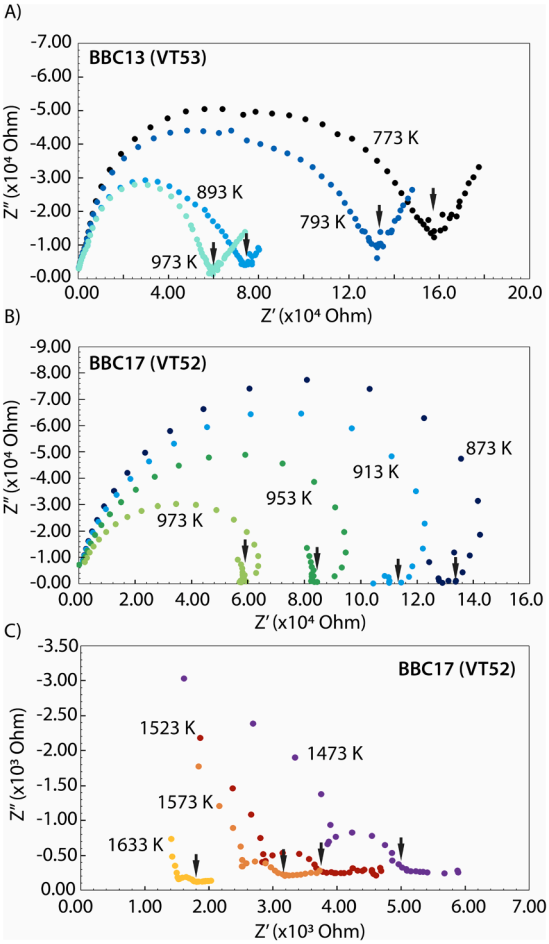

Fig. 4. Impedance spectra at selected temperatures for experiments A) BBC13 (S-free glass VT53), and B and C) BBC17 (S-bearing glass VT52). For both experiments, pressure is 2 GPa.

(Fig. 5**A**), but the activation energies of dry and hydrated tephritic, andesitic, or rhyolitic glasses range from 0.63 to 1.35 eV at pressures ≤ 3 GPa, with hydrogen decreasing ΔH (Gaillard, 2004; Pommier et al., 2008; Laumonier et al., 2015), similar to ΔH values in the present study.

The ΔH values found in the present work agree with the activation energies for Na tracer diffusion in silicate glasses and melts (e.g., Jambon, 1982; Henderson et al., 1985; Behrens, 1994; Lesher, 2010). The agreement is consistent with alkali ions (Na^{+}) being the major charge carriers, as is prevalent for silicate glasses (e.g., Terai, 1968; Shelby, 2020; Doremus, 1994). In contrast, the mobility of divalent cations (e.g., Ca^{2+}) in silicate glasses is much lower, and characterized by an activation energy ≥ 2.0 eV (Behrens, 1994; Natrup et al., 2005). The individual contribution of each charged species to bulk conductivity can be estimated using the tracer diffusion coefficient of each element (Appendix A). Estimates of the different ionic contributions to charge transport in our glasses emphasize the preponderant role of sodium cations that are almost entirely (>96%) responsible for bulk conductivity, while all other potential charge carriers have limited or negligible contributions. One possible exception is the S-rich glass VT55, for which sulfide could contribute up to 15% if S were not bonded to Si, a scenario that is not supported by the present work (see below).

The glass transition temperature (Tg) occurs at ~650–750 K for all samples, based on a small change in slope in Fig. 5 (e.g., Caillot et al., 1994). Tg corresponds to the temperature at which the electrical conductivity switches from an Arrhenius law (low T data) to a modified one. No clear effect of S on Tg is observed, though the highest Tg values tend to correspond to those of S-free glasses (VT53 and VT56). The non-Arrhenian temperature dependence of conductivity at T > Tg and until crystallization starts at ~973 K characterizes most samples. As previously observed (e.g., Souquet et al., 1998; Souquet, 2021), the departure from an Arrhenian behavior can be explained by local deformations of macromolecular chains, affecting the transfer of charges. In this model, the low-T activated mechanism remains significant above Tg, and an additional cooperative displacement mechanism becomes active as well (Caillot et al., 1994; Souquet et al., 1998). The following equation reflects both processes above Tg:

$$\sigma = A \times exp\left(\frac{-B_1}{R(T-T_2)} - \frac{B_2}{RT}\right) \quad (4)$$

Our conductivity values are fitted satisfactorily with Eq. (4), and optimized values of B_1, B_2, and T_2 are listed in Table 4. The energy term B_1 is very low (≤0.02 eV) compared to B_2 (0.07–0.34 eV). Comparison of the first and second exponential terms over the relevant temperature range indicates that the Arrhenian term is generally dominant. Over this T range, the conductivities of all samples are comparable, with the exception of BBC14 (VT54) (Fig. 5). This sample is significantly more conductive than the others, especially VT55, which has comparable S, alkali, and alkaline earth content (Table 3). The high conductivity of VT54 is likely an artefact caused by small amounts of graphite from the capsule, which were visible on the surface of the starting glass cylinder.

The onset of crystallization starts at ~973 K for all samples. It is very difficult to isolate the melt and crystal conductivity values based on bulk measurements once crystals have formed (Pommier et al., 2008). Therefore, the temperature was raised quickly (on the order of a few minutes) to reach higher temperatures (≥1373 K) where the melt phase is interconnected and dominates bulk conductivity. Above 1373 K, conductivities range from 5×10^{-2} to > 1 S/m and increase steeply with temperature. This behavior is consistent with a connected melt and a melt fraction that increases significantly with temperature. Based on melt fraction estimates using BSE images of quenched samples (e.g., Fig. S3), the melt conductivity at T_{quench} can be estimated. Assuming an interconnected melt phase and assuming a forsterite composition for the solid phase (Namur and Charlier, 2017), the Hashin-Shtrikman upper bound, derived from the effective medium theory, can be applied (e.g., Hashin and Shtrikman, 1962; Glover, 2015)

$$\sigma_{bulk} = \sigma_m\left(1 - \frac{3(1-X_m)(\sigma_m - \sigma_{fo})}{3\sigma_m - X_m(\sigma_m - \sigma_{fo})}\right) \quad (5)$$

with σ_{bulk} the bulk (measured) conductivity, X_m the melt fraction (0.5–0.7 at the time of quenching; see section 3.1), σ_m the melt conductivity, and σ_{fo} the conductivity of the forsterite crystals. The conductivity of forsterite comes from the study by ten Grotenhuis et al. (2005) for olivine aggregates with a 1.1 μm grain size, which is comparable to the grain size observed in our quenched samples (Fig. S3). Eq. (5) yields melt conductivities ranging from 0.7 to 2.2 S/m at T_{quench}, with S-free melt VT42 (BBC21) being least conductive and VT55 melt (BBC18) being most conductive. These values suggest that increasing S from 0 to ~5 wt% increases melt conductivity by a factor of 3. For a S content < 5 wt%, no clear effect on conductivity is observed.

We note that increasing pressure from 2 to 4 GPa has a relatively minor effect on bulk conductivity (see S-free glass VT56; Fig. 5). At 500 °C the conductivity of VT56 decreases from 3.3 to 2.1 S/m. This pressure effect is consistent with sodium cation hopping (e.g., Ryan and Smedley, 1984; Gaillard, 2004; Pommier et al., 2008; Ni et al., 2011a). Comparison with previous electrical studies of hydrous melts at comparable pressure and temperature conditions (Gaillard, 2004; Pommier et al., 2008; Ni et al., 2011b; Laumonier et al., 2015) shows that H-bearing melts are more conductive than the S-bearing melts in the present study (Fig. 5). The composition of the glasses from these previous studies is listed in Table S1.

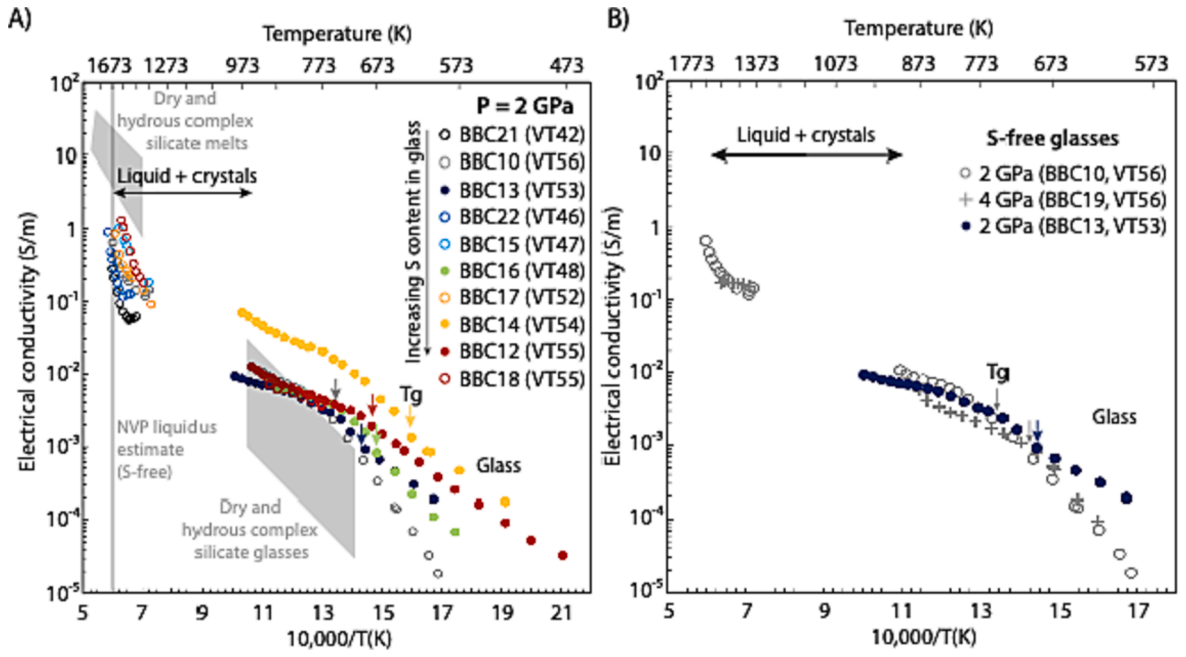

Fig. 5. Electrical conductivity for all experiments as a function of inverse temperature. A) Experiments at a pressure of 2 GPa. Vertical black arrows indicate a change in slope that corresponds to the glass transition (Tg), and the vertical grey line indicates the liquidus estimate of the S-free NVP composition at 1 GPa (after Namur and Charlier, 2017). Open circles: starting glass powders, filled circles: starting glass cylinders. Grey areas indicate electrical conductivity ranges from previous studies on dry and hydrous complex silicate glasses and melts (Gaillard, 2004; Pommier et al., 2008; Ni et al., 2011; Laumonier et al., 2015). B) Conductivity of S-free glasses VT56 and VT53, and effect of pressure on conductivity for S-free glass sample VT56, at 2 (grey circles) and 4 GPa (grey crosses).

Table 4
Summary of electrical experiments and activation energies for DC conductivity. (NA: not applicable; Tg: glass transition temperature; Tc: crystallization temperature). See Eqs. (3) and (4) for definition of other paramaters.

Run	Composition	S content (wt. %)*	P (GPa)	T_{quench} (K)	T < Tg			T > Tg and T < Tc				
					T range (K)	Ln (σ_0) (S/m)	ΔH (eV)	T range (K)	Ln (A) (S/m)	B_1 (eV)	B_2 (eV)	T_2 (K)
BBC21	VT42	0	2	1673	NA	NA	NA	NA	NA	NA	NA	NA
BBC13	VT53	0	2	1031	598–718	3.78	0.63	718–973	−3.24	0.02	0.07	575
BBC10	VT56	0	2	1669	593–750	11.0	1.10	750–884	−0.50	0.002	0.31	720
BBC19	VT56	0	4	1585	625–672	9.92	1.01	672–858	0.04	0.000	0.41	674
BBC22	VT46	0.1	2	1738	NA	NA	NA	NA	NA	NA	NA	NA
BBC15	VT47	1.2	2	1619	NA	NA	NA	NA	NA	NA	NA	NA
BBC16	VT48	1.7	2	874	573–694	8.06	0.88	694–874	−2.25	0.002	0.20	666
BBC17	VT52	3.8	2	1657	623–700	6.05	0.74	700–874	−3.10	0.004	0.10	669
BBC14	VT54	4.2	2	973	523–626	3.32	0.54	626–973	0.46	0.015	0.26	558
BBC12	VT55	4.8	2	944	475–667	2.95	0.55	667–944	−0.22	0.000	0.34	656
BBC18	VT55	4.8	2	1593	NA	NA	NA	673–893	−0.25	0.004	0.34	648

* From EMPA analyses onstarting glasses.

3.3. ^{29}Si NMR spectroscopy

The NMR spectra of starting glasses VT53 (S-free), VT48, 52, and 54 (S-bearing) are presented in Fig. 6. Starting glasses with added iron were not considered, because excessive quantities of paramagnetic Fe^{2+} cause severe peak broadening and strong spinning side bands (SSB) (Engelhardt and Michel, 1987 and references therein). Two components characterize the spectra of all samples. The major band with maximum located at −93.7 to −97.3 ppm can be attributed largely to a mixture of Q^3 and Q^4 species with shifts influenced by partial aluminum substitution (Engelhardt and Michel 1987), in agreement with previous studies of silicate glasses, with or without sulfur (e.g., Maekawa et al., 1991; Minami et al., 2000; Tsujimura et al., 2004). The small sharp peak at −62 ppm is attributed to very small amounts of crystalline olivine (e.g., Kanzaki and Xue, 2016). Forsterite olivine is the first liquidus phase in the NVP composition at low pressure (Namur and Charlier, 2017) and submicron-sized crystals likely formed during quenching of the glass, explaining why they were not visible in the BSE images. The small integral of this band relative to the rest of the ^{29}Si NMR spectrum indicates that such nanocrystals of olivine are present in very small amounts (<0.1 Si %).

Paramagnetic Mn^{2+} cations present in the samples analyzed by NMR reduce T1 spin–lattice relaxation times (Scholz and Thomas, 1995), and can also increase the ^{29}Si linewidth (Engelhardt and Michel, 1987). The quantity of Mn in the S-free glass VT53 (0.32 wt% MnO) is higher than in the other samples (0.04–0.13 wt%), and the additional amount may cause the pedestal for the main band (Fig. 6).

In typical S-free silicate glasses, as illustrated in Fig. S5 with a calcium-alumino-silicate (CAS) glass, the primary ^{29}Si band is typically symmetric with no peak shoulders, whereas in our glasses this symmetry is affected by the presence of an obvious broad shoulder on the high frequency side of the main band spanning a range from −35 to −70 ppm (Fig. 6). Sample VT52 exhibits the highest ^{29}Si intensity at ~−58 ppm. A shoulder at this frequency is inconsistent with silicon oxide Q^n species

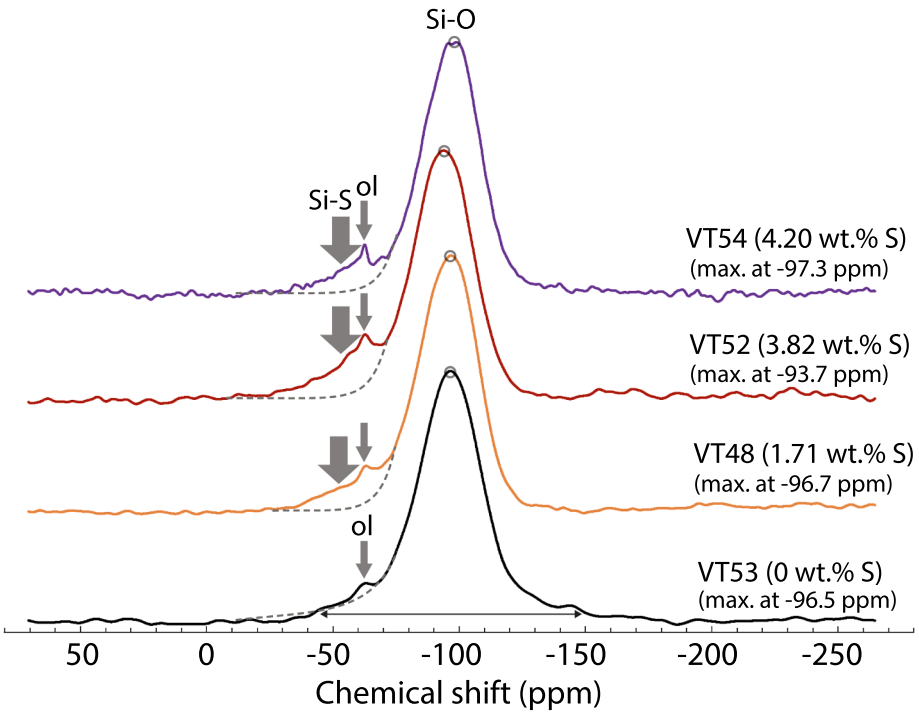

Fig. 6. ^{29}Si NMR results for starting glasses VT48, 52, 53 and 54. The grey circles indicate the maximum of the main peak (exact values are listed to the right). The dashed lines on the left side of the main peak are a mirror image of the right side of the same peak, highlighting the effects of Si–S bonds and quenched olivine crystals. The horizontal double arrow indicates the pedestal for glass VT53, possibly caused by relatively high Mn content.

for these compositions (Engelhardt and Michel, 1987). As has been previously observed for Na_2S-SiO_2 and Li_2S-SiS_2-Li_4SiO_4 oxysulfide glasses at ambient pressure (e.g., Asahi et al., 1999; Tatsumisago et al., 1996; Minami et al., 2000), Si–S bonds shift the ^{29}Si frequencies to higher values than for Si bonded only to oxygen. Specifically, a band centered at −50 to −60 ppm has been assigned to the chemical species $(SiO_3S)^{4-}$ (Hayashi et al., 2000). Spectral decomposition with Gaussian components (Fig. S6) reveals that the area of the shoulder in the case of VT52 is 14 ± 2% of the total silicon species. The composition of the same glass based on microprobe analysis indicates a S/Si atomic ratio of 12.1%, which is within the error limit of the value based on NMR spectroscopy. This agreement is consistent with (1) all, or nearly all, sulfide bonded to Si, and (2) few or no sulfide atoms bridging between two Si atoms. NMR results for VT48 bolster this analysis. For this sample, the S/Si percentage from EMPA is 5.0 mol.% and in the NMR spectrum the shoulder assigned to $(SiO_3S)^{4-}$ is ~50% the intensity of that observed for VT52 (Fig. 6). Sample VT54 is not in good agreement with the other sulfide-containing samples, because the area of the shoulder is smallest of the three, despite having the highest S/Si percentage (12.8 mol.%) from EMPA. The sample has less Ca than VT52, and less Mg than VT48, so the disagreement cannot be simply explained by proposing that alkaline metals disrupt bonding of sulfide to Si. Further study is needed to fully understand the area ratios in the NMR spectra.

The chemical shift at the maximum of the Si–O band reflects the mean degree of polymerization of the glass and can be compared with the amount of sulfide and alkaline metal content in the samples. In general, decreased polymerization of the sample (i.e., decrease in quantity of bridging oxygen atoms) causes the resonant frequency of ^{29}Si to increase, thereby causing the chemical shift to become less negative. Sample VT53 has no added S, and the maximum position of the $^{29}SiO_4$ band is at −96.5 ppm. Sample VT48 has minimal S (1.71 wt%) and the position of the band is unchanged (−96.7 ppm) within error of the fitting. Sample VT52 (3.82 wt% S) has a significantly less negative peak position (−93.7 ppm) which could suggest that the increased Si–S bonds are associated with decreased polymerization. However, an alternative explanation for the small shifts must be considered, because the addition of sulfide also causes a significant increase in the amount of Ca^{2+}, an established network modifier. The mol.% values of the two alkaline metals Mg^{2+} and Ca^{2+}, relative to SiO_2, are: VT53 (35%), VT48 (33%) and VT52 (46%). Therefore, the less negative value for δ at the band maximum is consistent with the greater alkaline metal content in sample VT52. Sample VT54, which has the most sulfide of the samples probed by NMR, has the most negative chemical shift (−97.3 ppm) but given significant broadening of the band (~30 ppm, full-width at half-maximum, FWHM) as well as slight asymmetry in the band shape, the <1 ppm difference in chemical shift relative to the sulfide-free sample VT53 (−96.5 ppm) is within error of the analysis. The alkaline metal content in VT54 (38 at.% of SiO_2) is nearly the same as for VT53, which reinforces the suggestion that the chemical shift of the main band can be rationalized in terms of network depolymerization arising from alkaline earth cations, without invoking a correlation to sulfide content.

3.4. Raman spectroscopy

Unpolarized Raman spectra of selected starting glasses and samples quenched after electrical experiments are shown over the 200–1250 cm^{-1} frequency range in Figs. 7 and 8. All glasses are luminescent, which is likely caused by the presence of transition metals (particularly Mn) and/or defects in the glass structure (e.g., Gaft et al., 2015). The Raman spectrum of starting glass VT55 containing approximately 5 wt% S is shown in Fig. 7 and compared with previous studies. The glass response is dominated by two broad bands with peak positions 550 and 1100 cm^{-1}. These bands reflect the silicate glass structure (e.g., McMillan and Piriou, 1983; Mysen and Frantz, 1992, 1994; Neuville and Mysen, 1996), particularly alkaline earth-bearing alumina silicate glasses (Merzbacher and White, 1991) that are most relevant to the present study. The low-frequency Raman band near 550 cm^{-1} has been assigned to the deformation vibration of Si–O–Si coupled with bending vibrations of tetrahedral O–Si–O (McMillan and Piriou, 1983). The high-frequency band near 1100 cm^{-1} is attributed to the symmetric Si–O stretching vibration of Q^3 species (e.g., Brawer and White, 1975, 1977; Moulton et al., 2021).

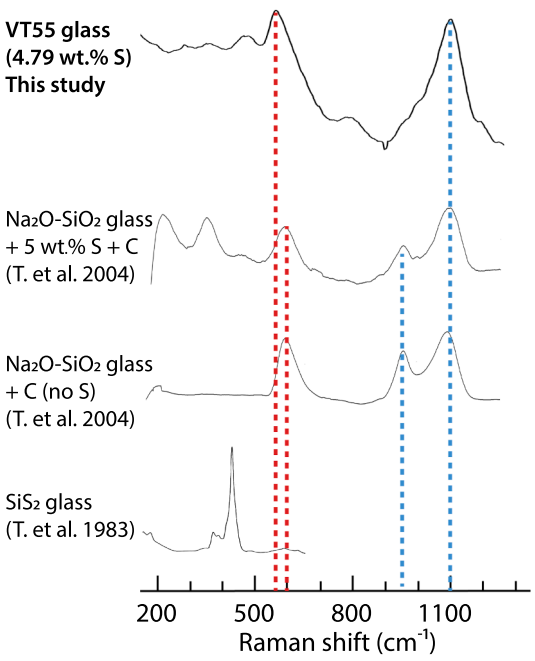

Fig. 7. Raman spectrum of a sulfide-rich silicate glass (VT55) acquired with 532-nm excitation. The spectrum is a spatial average and does not include PCA. Representative spectra from Tsujimura et al. (2004) and Tenhover et al. (1983) are also shown, with dashed vertical lines to aid comparison. See text for details.

Compared with S-free glasses, the most notable changes occur in the low-frequency region (<500 cm^{-1}), where several Raman bands with varying intensity are observed. Raman bands assigned to Si–S stretching modes in SiS_2 glasses have been measured near 430 and 370 cm^{-1} (Tenhover et al., 1983). Using density-functional theory (DFT), Devi et al. (2013) computed peak positions for SiS_2 and other Si–S glasses in the 200–600 cm^{-1} spectral window. Given extensive overlap of experimental and computed band positions assigned to various Si–S modes, with ones spanning the range 225–470 cm^{-1} which have been reported for MgS (niningerite) or mixed Mg/CaS samples (Avril et al., 2013), specific assignments to MgS, CaS, or Si–S are difficult. Nevertheless, based on the principal component spectra presented in Fig. 8, there is remarkable overlap between sample VT55/BBC18 and oldhamite from Avril et al. (2013), suggesting that clusters of CaS may be present in this sample. The decomposed spectra of VT52 show a prominent band at 330 cm^{-1} (starting glass) or 250 cm^{-1} (after electrical run BBC17). These features do not match spectra of niningerite or oldhamite. Possibly the peak positions reflect unique chemical structures (and vibrational modes) that are specific to our samples, e.g., Ca–S–Si, or Mg–S–Si. Interestingly, the amplitude of the principal component associated with sulfide-cation vibrations shows a high degree of spatial variation (see images in Fig. S7), perhaps providing additional support for spatial heterogeneity of sulfide distribution in the quenched sample. At this point, the preceding proposals are speculative, and it would also be premature to claim that our Raman spectra provide support for Si–S bonds in the quenched samples and starting materials. Prior Raman spectra of glasses acquired for a slightly reduced ($\Delta IW \sim +2.5$) S-bearing KSi_4O_9 glass (Klimm and Botcharnikov, 2010) or for more reduced ($\Delta IW < -1.5$) (Mg,Ca,Fe)S-bearing silicate melts (Namur et al., 2016a) found no indication of Si–S bonds. In addition, we see no evidence for Na-S bonds, which can be explained by the weak interactions between sodium and sulfide, and by the absence of Na_2S species at our highly reduced conditions (Anzures et al., 2020).

Forsterite was not observed in any of our Raman spectra, as evidenced by the absence of peaks in the 820–980 cm^{-1} range (e.g., Chopelas, 1991; McKeown et al., 2010). The NMR spectra showed that this phase is present in very small amounts in the bulk starting glasses (Section 3.3). Most likely, the sharp olivine doublet is missing in our Raman spectra because of the low concentration, or the spatial regions that were probed did not have this minor component in them.

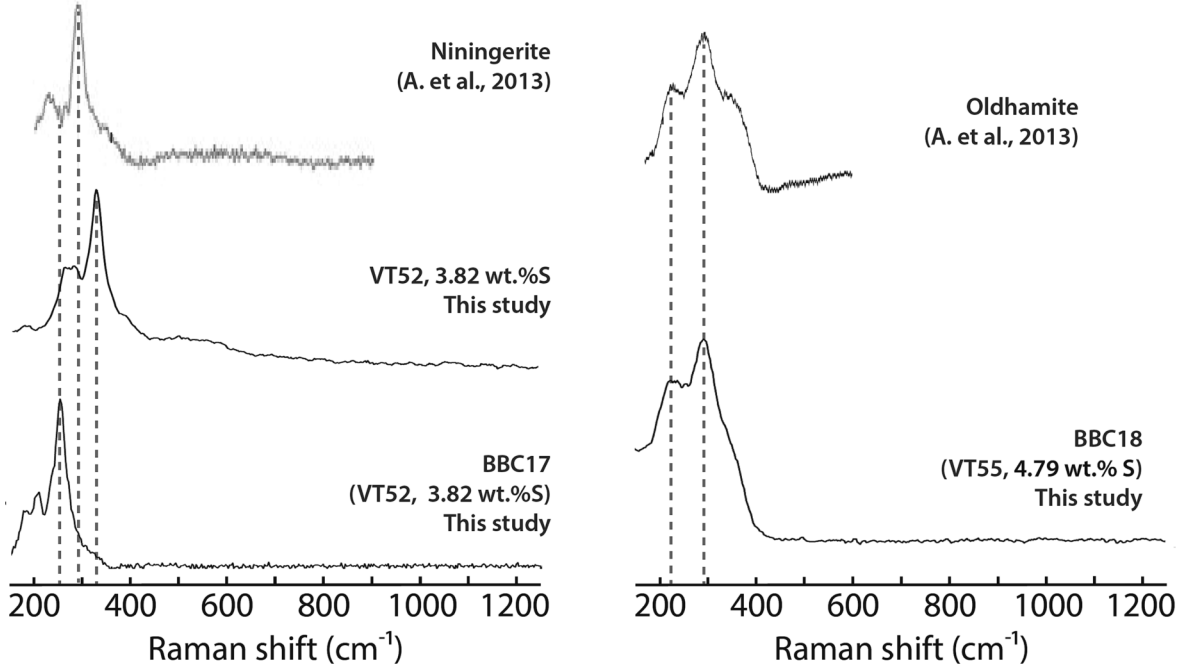

Fig. 8. Principal component spectra that highlight vibrational bands of sulfide bonded to alkaline-earth metals or silicon (–S–Ca, –S–Mg, –S–Si–O moieties). The samples are sulfide-rich glasses VT52 (before and after electrical experiment BBC17 performed at high pressure and temperature) and VT55. The spectrum of VT52 starting glass (middle left) is the same as Component 1 illustrated in Fig. S7. Spectra of Ca-rich and Mg-rich sulfides selected from Avril et al. (2013) are also shown for comparison.

3.5. Structure of highly reduced S-bearing alkali silicate glasses from a multi-spectroscopic approach

The complementary results from different spectroscopic techniques used in our study provide a multifaceted view of the role of sulfur on the structure and transport properties of highly reduced S-bearing glasses. Impedance spectroscopy highlights the mobility of charge carriers both in the glassy and partially molten states; ^{29}Si NMR spectroscopy provides direct insight regarding the interactions between S and the silica network; and Raman spectroscopy reveals interactions between S and alkaline earth elements.

The NMR results show that significant amounts of sulfur enter the silica framework by bonding with silicon, possibly even quantitative for two of the samples (VT48 and 52). Most or all of the S bound to Si is non-bridging, i.e., it can also interact with network modifier cations. Raman spectroscopy reveals alkaline earth-sulfides bonds, although the amount cannot be quantified. In general, alkaline earth elements are known to be strongly network modifying cations (e.g., Mysen and Richet, 2005), depolymerizing the structure of silicate glasses via the following scheme, where the equilibrium is strongly shifted to the right in the case of CaO:

$$\text{Si-O-Si} + \text{CaO} = \text{Si-O-Ca-O-Si} \quad (6)$$

For glasses of the present work, alkaline earth sulfides (CaS complexes) can modify the network in an analogous way:

$$\text{Si-O-Si} + \text{CaS} = \text{Si-O-Ca-S-Si} \quad (7)$$

Given that the bond energy (BE) of silicon oxide is considerably larger than that of silicon sulfide (e.g., BE_{SiO} of SiO_2 is 622 kJ/mol, and BE_{SiS} of SiS_2 is 533 kJ/mol; Holleman and Wiberg, 1995) it is reasonable to conclude that CaS is not as strong network modifier as CaO, i.e., the equilibrium reaction Eq. (7) is not as strongly driven to the right as in Eq. (6). In the case of Ca^{2+} added as a sulfide, our results from NMR and Raman spectroscopy indicate that CaS and Si–O–Ca–S–Si moieties coexist in the glasses, when prepared under highly reduced conditions. Regions rich with Ca–S or Mg–S bonds in the glass are also compatible with the chemical variations observed using WDS analyses. The heterogeneity in the spatial distribution of sulfide species can be seen as analogous to the micro-segregation of network modifiers that has been described in S-free alkaline-earth silicate glasses, where network former-rich regions coexist with network modifier-rich regions (Greaves, 1985; Ingram, 1987; Greaves and Ngai, 1995).

Although not directly probing the structure of glasses, electrical conductivity depends strongly on structural aspects (Martin, 2016) and provides information at the atomic scale about sulfide - cation interactions. Our electrical measurements show that samples with the highest S content (VT54 and VT55) can have conductivities ~3 times more than those without S. The larger ionic radius of S relative to O atoms imply weaker coulombic interactions with Na^+, therefore the mobility of Na^+ and bulk conductivity are enhanced in the presence of S (Ingram, 1987; Martin, 2016). Two arguments can explain why conductivity of our glasses is not uniformly correlated with S content: (1) the S content ranges from 0 to 5 wt%, which might not be sufficient to affect conductivity significantly (but this range was chosen for its relevance to Mercury lavas); (2) the S-rich glasses also have relatively high Ca content, causing competitive effects on conductivity because alkaline earth elements are known to impede the transport of Na^+ in aluminosilicate glasses (e.g., Shelby, 2020; Doremus, 1994). This argument is consistent with molecular dynamics and NMR studies (e.g., Cormack and Cao, 1996; Lee and Stebbins, 2003). The fact that the sample with the highest S content is ~3 times more conductive than the S-free glass suggests that the effect of sulfur may be quite strong, i.e., sufficient to overcome the effect of calcium on electrical conductivity.

3.6. Implication for Mercury

Quantifying Mercury's electrical conductivity-depth profile is a specific science objective of the ESA-JAXA BepiColombo mission because electrical conductivity can be used to describe the present-day thermal state and inform about planetary cooling (Genova et al., 2021). The transport properties of highly reduced S-rich silicate melts are required to understand and model the cooling history and dynamics of a young Mercury, when it hosted a magma ocean. Our samples are representative compositions from the Borealis Planitia region, and their electrical conductivity suggests that Mercury silicate melts are electrically less conductive than oxidized melts (Fig. 5**A**). Applied to the planet's early history, these observations imply that the expected low fO_2 conditions of the magma ocean enhanced its electrically insulating characteristic. Numerical convection models predict extremely high conductivity values for a convecting magma ocean to generate and sustain a dynamo (e.g., $>10^3$ S/m; Scheinberg et al., 2018). Given the low conductivity of Mercury's silicate melt, the magma ocean would have to be mostly composed of metal or to contain a large amount of graphite to reach conductivities $> 10^3$ S/m and generate a magnetic field. Present-day observations show that a dynamo is generated in the large metallic core. Whether an electrically insulating silicate shell influenced the internally generated magnetic field in the core remains to be investigated at the conditions of Mercury.

Our electrical results will help determine the relationship between conductivity and viscosity for S-bearing natural melts, which is useful to understand melt mobility at depth. Developing a laboratory-based model of electrical conductivity and viscosity of melts allows prediction of viscosity at low temperature (at the end of magma ocean crystallization) using electrical data (Pommier et al., 2013). Furthermore, probing melts with other spectroscopic methods (NMR and Raman spectroscopy) yields atomic insights that may overcome the challenge that viscosity and conductivity depend differently on composition, bonding, and other material properties. Laboratory experiments on reduced (IW-5) silicate melts showed that viscosity tends to decrease with increasing S content (Mouser et al., 2021), which would be consistent with depolymerization by S. A low-viscosity magma ocean would enhance convection, facilitating heat transport from the core. As a result, core cooling would be accelerated, affecting the magnetic field. Further experimental and theoretical studies of the electrical, thermal, and viscosity properties of a reduced magma ocean are needed to understand and model planetary differentiation and cooling.

4. Conclusions

We have synthesized highly reduced ($\Delta IW = -6$) sulfur-bearing silicate melts at temperatures of 1573–1673 K, and a pressure of ~1 bar. At these redox conditions, sulfur is present as S^{2-} (sulfide), and we have investigated its effect on the glass structure using different techniques: impedance spectroscopy at elevated pressure and temperature, electron microscopy, ^{29}Si NMR spectroscopy, and Raman spectroscopy.

Conductivity is a sensitive probe of ionic transport in glasses. Our results show that conductivity is significantly increased by S content, even in the small amounts representative of Mercury (<~5 wt%). ^{29}Si NMR spectroscopy supports the presence of Si–S bonds and for some samples, band areas suggest that nearly all S is bonded to Si. Regions rich with Ca–S or Mg–S bonds in the glass are identified using Raman spectroscopy to probe starting glasses and quenched materials from electrical experiments. Calcium sulfide appears to act as a network modifier, but one with a weaker effect than CaO.

Our study as well as the previous viscosity study of highly reduced S-rich silicate glasses and melts (Mouser et al., 2021) reveal the complex behavior of S on transport properties. Further work under pressure and temperature is needed to develop laboratory-based models of these properties that can then be applied to magma oceans and mantle-derived melts. Such models shed light on the evolution of Mercury

during differentiation and will contribute to the interpretation of data expected from the ESA-JAXA Bepi-Colombo mission.

Declaration of Competing Interest

The authors declare that they have no known competing financial interests or personal relationships that could have appeared to influence the work reported in this paper.

Acknowledgments

AP thanks Olivier Namur, Mike Walter, and Dionysis Foustoukos for fruitful discussions, Carnegie-EPL librarians Shaun Hardy and M.A. O'Donnell for their assistance, and the Carnegie-EPL Facilities team for their invaluable support. Use of the COMPRES Cell Assembly Project was supported by COMPRES under NSF Cooperative Agreement EAR-1661511. AP acknowledges financial support from NSF-CAREER award EAR-1750746 and the Carnegie endowment. BC is a Research Associate of the Belgian Fund for Scientific Research-FNRS. The NMR spectroscopy was performed at the W.M. Keck Solid State NMR facility (at EPL) that received support from the W. M. Keck Foundation, the NSF, and Carnegie Science. The authors thank editor S. K. Lee, R. F. Cooper, Y. Li, and an anonymous reviewer for helpful comments.

Data Availability

The experimental data used in the figures are available through Dryad at: https://doi.org/10.6076/D1TP4S.

Appendix A. Determination of the contribution of different monovalent cations to the bulk conductivity of glasses

Conductivity in our silicate glasses is ionic. Electronic conductivity due to iron is negligible because our glasses are either Fe-free or contain very small amounts of iron and Si^0 (Table 3). Conductivity by electrons was also found negligible in sulfide glasses (Na_2S-SiS_2 and K_2S-SiS_2) (Ravaine, 1980). The contribution of each element *i* to the bulk conductivity can be estimated using the Nernst-Einstein equation (e.g., Terai, 1968; Souquet and Perera, 1990; Gaillard, 2004; Pommier et al., 2008):

$$\sigma_i = \frac{x_i \times q^2 \times D_i}{k_B \times T \times H_r} \quad \text{(A1)}$$

with σ_{bulk} the bulk conductivity, σ_i the conductivity of charge carrier *i*, x_i the number of charge carriers per unit volume, q its charge, D_i the tracer diffusion coefficient of *i*, k_B the Boltzmann constant, T the temperature, and H_r the Haven ratio. In silicate glasses with high Na^+ contents, H_r ranges from 0.44 to 0.55 (Souquet, 2021). Here we assume an intermediate value of 0.50.

Alkali (Na^+ and K^+), major alkaline earth (Ca^{2+} and Mg^{2+}), and sulfide are considered possible charge carriers in the glasses of the present study. For each possible charge carrier, diffusion coefficients are from tracer diffusion studies: Terai (1968) and Jambon (1982) for Na^+, Jambon and Carron (1976) for K^+, Behrens (1994) and Natrup et al. (2005) for Ca^{2+} (the same D values were used for Mg^{2+}), and Lierenfeld et al. (2018) for S^{2-}. At a defined temperature, the conductivity of each element (σ_i) is calculated using Eq. (A1) and the individual contributions are obtained by comparison with the measured conductivity.

Although the presence of Si^{2+} has been invoked in reduced glasses (Cooper et al., 2010), the tracer diffusion coefficient of silicon is extremely low ($\sim 3.10^{-22}$ m^2/s at 1073 K in an aluminosilicate glass; Lepke et al., 2013). Similarly, aluminum has very low D values ($<10^{-22}$ m^2/s below Tg; Lepke et al., 2013). As a result, we did not consider Si and Al as plausible charge carriers in our glasses. Oxygen is part of the silica network and is not expected to contribute to the transfer of charges. However, if O^{2-} were diffusing in the glasses, its contribution would be insignificant because its D value ($\sim 10^{-20}$ m^2/s at 873 K; after Lepke et al., 2013) is several orders of magnitude lower than that of alkali, alkaline earth and sulfur (respectively $\sim 10^{-12}$, $\sim 10^{-17}$, and 2.10^{-13} m^2/s at 873 K).

As an example, at 873 K, the contribution of sodium cations to bulk conductivity ranges from 96.5 to 99.9% depending on the experiment considered, and sulfur anions represent the second major contributor with 0–3.5%. One exception is experiment BBC12 (VT55 glass), with estimated contributions of Na^+ and S^{2-} of 85.5% and 15%, respectively. The estimate for the contribution of sulfur is an upper limit because most sulfur enters the silica framework (Section 3.3) and thus does not contribute to charge transport. The contributions of network modifiers potassium, calcium, and magnesium cations amount to less than 1%, in agreement with previous studies on dry and hydrous silicate glasses (e.g., Gaillard, 2004; Pommier et al., 2008).

Appendix B. Supplementary material

The supplementary material includes: method for estimating conductivity error; drawings of electrical cell assemblies; time-temperature paths and power-temperature curves for electrical experiments; an example of image analysis using software ImageJ; back-scattered electron (BSE) images and wavelength dispersive spectroscopy (WDS) maps of quenched sample BBC22; the ^{29}Si NMR spectrum of a CAS glass; Raman spectra and images for starting glass VT52. Supplementary material to this article can be found online at https://doi.org/10.1016/j.gca.2023.10.027.

References

Ackerson, M.R., Cody, G.C., Mysen, B.O., 2020. ^{29}Si solid state NMR and Ti K-edge XAFS pre-edge spectroscopy reveal complex behavior of Ti in silicate melts. Prog. Earth Planet. Sci. 7, 14.

Anzures, B.A., Parman, S.W., Milliken, R.E., Namur, O., Cartier, C., Wang, S., 2020. Effect of sulfur speciation on chemical and physical properties of very reduced mercurian melts. Geochim. Cosmochim. Acta 286, 1–18.

Asahi, T., Miura, Y., Nanba, T., Yamashita, H., 1999. Chemical bonding state of sulfur in oxysulfide glasses. Korean J. Ceramics 5, 178–182.

Avril, C., Malavergne, V., Caracas, R., Zanda, B., Reynard, B., Charon, E., Bobocioiu, E., Brunet, F., Borensztajn, S., Pont, S., Tarrida, M., Guyot, F., 2013. Raman spectroscopic properties and Raman identification of CaS-MgS-MnS-FeS-Cr_2FeS_4 sulfides in meteorites and reduced sulfur-rich systems. Meteorit. Planet. Sci. 48, 1415–1426.

Baker, D., Moretti, R., 2011. Modeling the solubility of sulfur in magmas: A 50-year old geochemical challenge. Rev. Mineral. Geochem. 73, 167–213.

Behrens, H., 1994. Na and Ca tracer diffusion in plagioclase glasses and supercooled melts. Chem. Geol. 96, 267–275.

Brawer, S.A., White, W.B., 1975. Raman spectroscopic investigation of the structure of silicate glasses (I). The binary alklai silicates. J. Chem. Phys. 63, 2421–2432.

Brawer, S.A., White, W.B., 1977. Raman spectroscopic investigation of the structure of silicate glasses (II). Soda-alkaline earth-alumina ternary and quaternary glasses. J. Non-Cr. Sol. 23, 261–278.

Buono, A.S., Walker, D., 2011. The Fe-rich liquidus in the Fe–FeS system from 1 bar to 10 GPa. Geochim. Cosmochim. Acta 75, 2072–2087.

Caillot, E., Duclot, M.J., Souquet, J.-L., et al., 1994. A unified model for ionic transport in alkali disilicates below and above the glass transition. Phys. Chem. Glasses 35, 22–27.
Carroll, M.R., Rutherford, M.J., 1988. Sulfur speciation in hydrous experimental glasses of varying oxidation states: Results from measured wavelength shifts of sulfur X-rays. Am. Min. 73, 845–849.
Charlier, B., Namur, O., 2019. The origin and differentiation of planet Mercury. Elements 15, 9–14.
Chopelas, A., 1991. Single crystal Raman spectra of forsterite, fayalite, and monticellite. Am. Mineral. 76, 1101–1109.
Cooper, R.F., Everman, R.L.A., Hustoft, J.W., Shim, S.-H.-D., 2010. Mechanism and kinetics of reduction of a FeO-Fe_2O_3-CaO-MgO aluminosilicate melt in a high-CO-activity environment. Am. Mineral. 95, 810–824.
Cormack, A.N., Cao, Y., 1996. Molecular dynamics simulation of silicate glasses. Mol. Eng. 6, 183–227.
Darken, L.S., Gurry, R.W., 1945. The system iron-oxygen I. the wüstite field and related equilibria. J. Am. Chem. Soc. 67, 1398–1412.
Devi, V.R., Zabidi, N.A., Shrivastava, K.N., 2013. Interpretation of the Raman spectra of the glassy states of Si_xS_{1-x} and Si_xSe_{1-x}. Mat. Chem. Phys. 141, 651–656.
Doremus, R.H., 1994. Glass Science, 2nd edition, 352 pp., ISBN: 978-0-471-89174-1.
Engelhardt, G., Michel, D., 1987. High-resolution sild-state NMR of silicates and zeolites. 485 pp., John Wiley & Sons. ISBN-10: 0471915971.
Eugster, H.P., Wones, D.R., 1962. Stability relations of the ferruginous biotite, annite. J. Petrol. 3, 82–125.
Evans, L.G., et al., 2012. Major-element abundances on the surface of Mercury: Results from the MESSENGER Gamma-Ray Spectrometer. J. Geophys. Res. 117, E00L07.
Fincham, C.J.B., Richardson, F.D., 1954. The behavior of sulphur in silicate and aluminate melts. Proc. R. Soc. Lond. A 223, 40–62.
Fleet, M.E., Liu, X., Harmer, S.L., King, P.L., 2005. Sulfur K-edge XANES spectroscopy: Chemical state and content of sulfur in silicate glasses. Can. Mineral. 43, 1605–1618.
Gaft, M., Reisfeld, R., Panczer, G., 2015. Modern Luminescence Spectroscopy of Minerals and Materials, Springer, 625 pp.
Gaillard, F., 2004. Laboratory measurements of electrical conductivity of hydrous and dry silicic melts under pressure. Earth Planet. Sci. Lett. 218 (1–2), 215–228.
Genova, A., et al., 2021. Geodesy, Geophysics and Fundamental Physics Investigations of the BepiColombo Mission. Space Sci. Rev. 217, 31.
Glover, P.W.J., 2015. Geophysical Properties of the Near Surface Earth: Electrical Properties, second ed. Treatise on Geophysics, pp. 89–137.
Greaves, G.N., 1985. EXAFS and the structure of glass. J. Non-Cr. Sol. 71 (1–3), 203–217.
Greaves, G.N., Ngai, K.L., 1995. Relating the atomic structure of alumino-silicate glasses to their ionic transport properties. J. Non-Cr. Sol. 192–193, 405–410.
Hashin, Z., Shtrikmann, S., 1962. A variational approach to the theory of the effective magnetic permeability of multiphase materials. J. Appl. Phys. 33, 3125–3131.
Hayashi, A., Araki, R., Komiya, R., Tadanaga, K., Tatsumisago, M., Minami, T., 1998. Thermal and electrical properties of rapidly quenched Li_2S-SiS_2-Li_2O-P_2O_5 oxysulfide glasses. Solid State Ionics 113–115, 7338–7738.
Hayashi, A., Tatsumisago, M., Minami, T., 2000. Crystallization process of lithium oxysulfide glasses. J. Non-Cr. Sol. 276, 27–34.
Henderson, P., Nolan, J., Cunningham, G.C., Lowry, R.K., 1985. Structural control and mechanisms of diffusion in natural silicate melts. Contrib. Mineral. Petrol. 89 (2–3), 263–272.
Herd, C.D.K., 2008. Basalts as probes of planetary interior redox state. Rev. Mineral. Geochem. 68, 527–553.
Hirai, K., Tatsumisago, M., Minami, T., 1995. Thermal and electrical properties of rapidly quenched glasses in the systems Li_2S-SiS_2-Li_xMO_y (Li_xMO_y = Li_4SiO_4, Li_2SO_4). Solid State Ionics 78, 269–273.
Holleman, A.F., Wiberg, E., 1995. Inorganic Chemistry, de Gruyter, 1884 pp., ISBN 0-12-352651-5.
Iacovino, K., McCubbin, F.M., Vander Kaaden, K.E., Clark, J., Wittmann, A., Jakubek, R. S., Moore, G.M., Fries, M.D., Archer, D., Boyce, J.W., 2023. Carbon as a key driver of super-reduced explosive volcanism on Mercury: Evidence from graphite-melt smelting experiments. Earth Planet. Sci. Lett. 602, 117908.
Ingram, M.D., 1987. Ionic conductivity in glass. Phys. Chem. Glasses 28 (6), 215–268.
Izenberg, N.R., Klima, R.L., Murchie, S.L., Blewett, D.T., Holsclaw, G.M., McClintock, W. E., Malaret, E., Mauceri, C., Vilas, F., Sprague, A.L., Helbert, J., Domingue, D.L., Head III, J.W., Goudge, T.A., Solomon, S.C., Hibbitts, C.A., Dyar, M.D., 2014. The low-iron, reduced surface of Mercury as seen in spectral reflectance by MESSENGER. Icarus 228, 364–374.
Jambon, A., 1982. Tracer diffusion in granitic melts: Experimental results for Na, K, Rb, Cs, Ca, Sr, Ba, Ce, Eu, to 1300 °C and a model of calculation. J. Geophys. Res. 87 (B13), 10797–10810.
Jambon, A., Carron, J.-P., 1976. Diffusion of Na, K, Rb, and Cs in glasses of albite and orthoclase composition. Geochim. Cosmochim. Acta 40, 897–903.
Kanzaki, M., Xue, X., 2016. Cation distribution in Mg-Zn olivine solid solution: a Si-29 MAS NMR and first-principles calculation study. J. Mineral. Petrol. Sci. 111 (4), 292–296.
Klimm, K., Botcharnikov, R.E., 2010. The determination of sulfate and sulfide species in hydrous silicate glasses using Raman spectroscopy. Am. Mineral. 95, 1574–1579.
Klimm, K., Kohn, S.C., O'Dell, L.D., Botcharnikov, R.E., Smith, M.E., 2012. The dissolution mechanism of sulphur in hydrous silicate melts. I: Assessment of analytical techniques in determining the sulphur speciation in iron-free to iron-poor glasses. Chem. Geol. 322–323, 237–249.
Laumonier, M., Gaillard, F., Sifre, D., 2015. The effect of pressure and water concentration on the electrical conductivity of dacitic melts: Implication for magnetotelluric imaging in subduction areas. Chem. Geol. 418, 66–76.
Lee, S.K., Stebbins, J.F., 2003. Nature of Cation Mixing and Ordering in Na-Ca Silicate Glasses and Melts. J. Phys. Chem. B 2003 (107), 3141–3148.
Lepke, et al., 2013. Oxygen-18, aluminium-26 and silicon-30 self diffusion in aluminosilicate glasses. Phys. Chem. Glasses: Eur. J. Glass Sci. Technol. B 54 (1), 15–19.
Lesher, C.E., 2010. Self-diffusion in silicate melts: theory, observations and applicatiobs to magnatic systems. Rev. Mineral. Geochem. 72, 269–309.
Lierenfeld, M.B., Zajacz, Z., Bachmann, O., Ulmer, P., 2018. Sulfur diffusion in dacitic melt at various oxidation states: Implications for volcanic degassing. Geochim. Cosmochim. Acta 226, 50–68.
Lonergan, J.M., Lonergan, C., Silverstein, J., Cholsaipant, P., McCloy, J., 2020. Thermal properties of sodium borosilicate glasses as a function of sulfur content. J. Am. Ceram. Soc. 103 (6), 3610–3619.
Maekawa, H., Maekawa, T., Kawamura, K., Yokokawa, T., 1991. The structural groups of alkali silicate glasses determined from ^{29}Si MAS-NMR. J. Non-Cryst. Solids 127, 53–64.
Malavergne, V., Toplis, M.J., Berthet, S., Jones, J., 2010. Highly reducing conditions during core formation on Mercury: implications for internal structure and the origin of a magnetic field. Icarus 206, 199–209.
Martin, S.W., 2016. Glass and glass-ceramic sulfide and oxy-sulfide solid electrolytes. Chapter 14 in Handbook of Solid State Batteries 2nd Edition edited by Dudney, N.J., West, W.C., Nanda, J. World Scientific.
McCoy, T.J., Peplowski, P.N., McCubbin, F.M., Weider, S.Z., Solomon, S.C., Nittler, L.R., Anderson, B.J., 2018. The geochemical and mineralogical diversity of Mercury. In: Mercury, the View After MESSENGER. Cambridge University Press, pp. 176–190.
McCubbin, F.M., Riner, M.A., Vander Kaaden, K.E., Burkemper, L.K., 2012. Is Mercury a volatile-rich planet? Geophys. Res. Lett. 39.
McKeown, D.A., Bell, M.I., Caracas, R., 2010. Theoretical determination of the Raman spectra of single-crystal forsterite (Mg2SiO4). Am. Mineral. 95, 980–986.
McMillan, P., Piriou, B., 1983. Raman spectroscopic studies of silicate and related glass structure - a review. Bull. Mineral. 106, 57–75.
Merzbacher, C.I., White, W.B., 1991. The structure of alkaline earth aluminosilicate glasses as determined by vibrational spectroscopy. J. Non-Cr. Sol. 130, 18–34.
Minami, T., Hayashi, T., Tatsumisago, M., 2000. Preparation and characterization of lithium ion-conducting oxysulfide glasses. Solid State Ionics 136–137, 1015–1023.
Moulton, B.J.A., Silva, L.D., Doerenkamp, C., Lozano, H., Zanotto, E.D., Eckert, H., Pizani, P.S., 2021. Speciation and polymerization in a barium silicate glass: Evidence from ^{29}Si NMR and Raman spectroscopies. Chem. Geol. 586, 120611.
Mouser, M.D., Dygert, N., Anzures, B.A., Grambling, N.L., Hrubiak, R., Kono, Y., et al., 2021. Experimental investigation of Mercury's magma ocean viscosity: Implications for the formation of Mercury's cumulate mantle, its subsequent dynamic evolution, and crustal petrogenesis. J. Geophys. Res.: Planets 126.
Mysen, M.O., Richet, P., 2005. Silicate Glasses and Melts, Properties and Structure, 544 pp., Elsevier, Amsterdam, Netherlands.
Mysen, B.O., Frantz, J.D., 1992. Raman spectroscopy of silicate melts at magmatic temperatures: Na_2O-SiO_2, K_2O-SiO_2 and Li_2O-SiO_2 binary compositions in the temperature range 25–1475°C. Chem. Geol. 96, 321–332.
Mysen, B.O., Frantz, J.D., 1994. Silicate melts at magmatic temperatures: in-situ structure determination to 1651 °C and effect of temperature and bulk composition on the mixing behavior of structural units. Contrib. Mineral. Petrol. 117, 1–14.
Namur, O., Charlier, B., 2017. Silicate mineralogy at the surface of Mercury. Nat. Geosci. 10, 9–13.
Namur, O., Charlier, B., Holtz, F., Cartier, C., McCammon, C., 2016a. Sulfur solubility in reduced mafic silicate melts: implications for the speciation and distribution of sulfur on Mercury. Earth Planet. Sci. Lett. 448, 102–114.
Namur, O., Collinet, M., Charlier, B., Grove, T.L., Holtz, F., McCammon, C., 2016b. Melting processes and mantle sources of lavas on Mercury. Earth Planet. Sci. Lett. 439, 117–128.
Natrup, F.V., Bracht, H., Murugavel, S., Roling, B., 2005. Cation diffusion and ionic conductivity in soda-lime silicate glasses. Phys. Chem. Chem. Phys. 7, 2279–2286.
Neuville, D.R., Mysen, B.O., 1996. Role of aluminium in the silicate network: In situ, high-temperature study of glasses and melts on the join SiO_2-$NaAlO_2$. Geochim. Cosmochim. Acta 60 (10), 1727–1737.
Ni, H., Keppler, H., Manthilake, G., Katsura, T., 2011a. Electrical conductivity of dry and hydrous $NaAlSi_3O_8$ glasses and liquids at high pressures. Contrib. Mineral. Petrol. 162, 501–513.
Ni, H., Keppler, H., Behrens, H., 2011b. Electrical conductivity of hydrous basaltic melts: implications for partial melting in the upper mantle. Contrib. Mineral. Petrol. 162, 637–650.
Nittler, L.R., Starr, R.D., Weider, S.Z., McCoy, T.J., Boynton, W.V., Ebel, D.S., Ernst, C.M., Evans, L.G., Goldsten, J.O., Hamara, D.K., Lawrence, D.J., McNutt, R.L., Schlemm, C. E., Solomon, S.C., Sprague, A.L., 2011. The major-element composition of Mercury's surface from MESSENGER X-ray spectrometry. Science 333, 1847–1850.
Nittler, L.R., Chabot, N.L., Grove, T.L., Peplowski, P.N., 2018. The chemical composition of Mercury. In: Solomon, S.C., Nittler, L.R., Anderson, B.J. (Eds.), Mercury: The View after MESSENGER, vol. 3. Cambridge University Press.
O'Neill, H.St.C., Mavrogenes, J.A., 2002. The sulfide capacity and the sulfur content at sulfide saturation of silicate melts at 1400°C and 1 bar. J. Petrol. 43, 1049–1087.
O'Neill, H.St.C., Mavrogenes, J.A., 2022. The sulfate capacities of silicate melts. Geochim. Coscmochim. Acta 334, 368–382.
Peplowski, P.N., Evans, L.G., Stockstill-Cahill, K.R., Lawrence, D.J., Goldsten, J.O., McCoy, T.J., et al., 2014. Enhanced sodium abundance in Mercury's north polar region revealed by the MESSENGER Gamma-Ray Spectrometer. Icarus 228, 86–95.
Peplowski, P.N., Lawrence, D.J., Feldman, W.C., Goldsten, J.O., Bazell, D., Evans, L.G., Head, J.W., Nittler, L.R., Solomon, S.C., Weider, S.Z., 2015. Geochemical terranes of

Mercury's northern hemisphere as revealed by MESSENGER neutron measurements. Icarus 253, 346–363.
Pommier, A., Gaillard, F., Pichavant, M., Scaillet, B., 2008. Laboratory measurements of electrical conductivities of hydrous and dry Mount Vesuvius melts under pressure. J. Geophys. Res. 113, B05205.
Pommier, A., Evans, R.L., Key, K., Tyburczy, J.A., Mackwell, S., Elsenbeck, J., 2013. Prediction of silicate melt viscosity from electrical conductivity: A model and its geophysical implications. Geophys. Geosyst. Geochem. 14.
Pommier, A., Leinenweber, K., 2018. Electrical cell assembly for reproducible conductivity experiments in the multi-anvil. Am. Mineral. 103, 1298–1305.
Pradel, A., Ribes, M., 2014. Ionic conductivity of chalcogenide glasses. In: Adam, J.-L., Zhang, X. (Eds.), Chapter 7 in Chalcogenide Glasses - Preparation, Properties and Applications. Woodhead Publishing, pp. 16–208.
Ravaine, D., 1980. Glasses as solid electrolytes. J. Non-Cryst. Solids 38–39, 353–358.
Renggli, C.J., Klemme, S., Morlok, A., Berndt, J., Weber, I., Hiesinder, H., King, P.L., 2022. Sulfides and hollows formed on Mercury's surface by reactions with reducing S-rich gases. Earth Planet. Sci. Lett. 593, 117647.
Ribes, M., Ravaine, D., Souquet, J.L., Maurin, M., 1979. Synthèse, structure et conduction ionique de nouveaux verres à base de sulfures. Rev. Chim. Min. 16, 339–348.
Ryan, M.J., Smedley, S.I., 1984. The effect of pressure on fast ion conductivity in glasses. J. Non-Cryst. Sol. 65, 29–37.
Saxena, S., Pommier, A., Tauber, M.J., 2021. Iron sulfides and anomalous electrical resistivity in cratonic environments. J. Geophys. Res.: Solid Earth 126.
Scheinberg, A.L., Soderlund, K.M., Elkins-Tanton, L., 2018. A basal magma ocean dynamo to explain the early lunar magnetic field. Earth Planet. Sci. Lett. 492, 144–151.
Scholz, K., Thomas, B., 1995. Measurements of spin-lattice relaxation times, T_1, in Na_2O-MgO-SiO_2 glasses doped with MnO. Sol. State Nucl. Magn. Res. 4, 309–311.
Shelby, J.E., 2020. Introduction to Glass Science and Technology, 3rd ed., Royal Society of Chemistry, 326 pp.
Souquet, J.L., Perera, W.G., 1990. Thermodynamics applied to ionic transport in glasses. Solid State Ionics 40–41, 595–604.
Souquet, J.L., Duclot, M., Levy, M., 1998. Ionic transport mechanisms in oxide-based glasses in the supercooled and glassy states. Solid State Ionics 105, 237–242.
Souquet, J.-L., 2021. Ionic and electronic transport, Chapter 4.2, pp. 453–463. In: Encyclopedia of Glass Science, Technology, History, and Culture, Volume I, First Edition, Ed: Pascal Richet, The American Ceramic Society. John Wiley & Sons, Inc.
Stebbins, J.F., 1987. Identification of multiple structural species in silicate glasses by ^{29}Si NMR. Nature 330, 465–467.
Steele, A., Fries, M.D., Amundsen, H.E.F., Mysen, B.O., Fogel, M.L., Schweizer, M., Boctor, N.Z., 2007. Comprehensive imaging and Raman spectroscopy of carbonate globules from Martian meteorite ALH 84001 and a terrestrial analogue from Svalbard. Meteor. Planet. Sci. 42 (9), 1549–1566.
Steele, A., McCubbin, F.M., Fries, M.D., et al., 2012. A reduced organic carbon component in martian basalts. Science 337 (6091), 212–215.
Tatsumisago, T., Hirai, K., Hirata, T., Takahashi, M., Minami, T., 1996. Structure and properties of lithium ion conducting oxysulfide glasses prepared by rapid quenching. Solid State Ionics 86–88, 487–490.
Tatsumisago, M., Yamashita, H., Hayashi, A., Morimoto, H., Minami, T., 2000. Preparation and structure of amorphous solid electrolytes based on lithium sulfide. J. Non-Cryst. Solids 274, 30–38.
ten Grotenhuis, S.M., Drury, M.R., Spiers, C.J., Peach, C.J., 2005. Melt distribution in olivine rocks based on electrical conductivity measurement. J. Geophys. Res. 110, B12201.
Tenhover, M., Hazle, M.A., Grasselli, R.K., 1983. Atomic structure of SiS_2 and $SiSe_2$ glasses. Phys. Rev. Lett. 51, 404–406.
Terai, R., 1968. Self-diffusion of sodium ions and electrical conductivity in sodium aluminosilicate glasses. J. Ceram. Assoc. Jpn. 76, 189–197.
Tsujimura, T., Xue, X., Kanzaki, M., Walter, M.J., 2004. Sulfur speciation and network structural changes in sodium silicate glasses: Constraints from NMR and Raman spectroscopy. Geochim. Cosmochim. Acta 68 (24), 5081–5101.
Vander Kaaden, K.E., McCubbin, F.M., Nittler, L.R., Peplowski, P.N., Weider, S.Z., Frank, E.A., McCoy, T.J., 2017. Geochemistry, mineralogy, and petrology of boninitic and komatiitic rocks on the mercurian surface: Insights into the mercurian mantle. Icarus 285, 155–168.
Watson, D.E., Martin, S.W., 2017. Short range order characterization of the Na2S + SiS2 glass system using Raman, infrared and 29Si magic angle spinning nuclear magnetic resonance spectroscopies. J. Non-Cryst. Solids 471, 39–50.
Weider, S.Z., Nittler, L.R., Starr, R.D., Crasper-Pregont, E.J., Peplowski, P.N., Denevi, B. W., et al., 2015. Evidence of geochemical terranes on Mercury: the first global mapping of major elements on the surface of the innermost planet. Earth Planet. Sci. Lett. 416, 109–120.
Wilke, M., Klimm, K., Kohn, S.C., 2011. Spectroscopic studies on sulfur speciation in synthetic and natural glasses. Rev. Mineral. Geochem. 73, 41–78.
Zolotov, M.Y., Sprague, A.L., Hauck, S.A., Nittler, L.R., Solomon, S.C., Weider, S.Z., 2013. The redox state, FeO content, and origin of sulfur-rich magmas on Mercury. J. Geophys. Res. Planets 118, 138–146.